# Ammonium nitrate particles formed in upper troposphere sourced from ground ammonia during Asian monsoons

Michael Höpfner[1], Jörn Ungermann[2], Stephan Borrmann[3,4], Robert Wagner[1], Reinhold Spang[2], Martin Riese[2,5], Gabriele Stiller[1], Oliver Appel[3,4], Anneke M. Batenburg[3,4], Silvia Bucci[6], Francesco Cairo[7], Antonis Dragoneas[3,4], Felix Friedl-Vallon[1], Andreas Hünig[3,4], Sören Johansson[1], Lukas Krasaukas[2], Bernard Legras[6], Thomas Leisner[1], Christoph Mahnke[3,4], Ottmar Möhler[1], Sergej Molleker[3,4], Rolf Müller[2], Tom Neubert[8], Johannes Orphal[1], Peter Preusse[2], Markus Rex[9], Harald Saathoff[1], Fred Stroh[2], Ralf Weigel[4], and Ingo Wohltmann[9]

[1]Institute of Meteorology and Climate Research, Karlsruhe Institute of Technology, Karlsruhe, Germany

[2]Institute of Energy and Climate Research, Stratosphere, Forschungszentrum Jülich, Jülich, Germany

[3]Department for Particle Chemistry, Max Planck Institute for Chemistry, Mainz, Germany

[4]Institute for Atmospheric Physics, Johannes Gutenberg University, Mainz, Germany

[5]Institute for Atmospheric and Environmental Research, University of Wuppertal, Wuppertal, Germany

[6]Laboratoire de Météorologie Dynamique, UMR8539, IPSL, CNRS/PSL-ENS/Sorbonne Université/École polytechnique, Paris, France

[7]Institute of Atmospheric Sciences and Climate, ISAC-CNR, Rome, Italy

[8]Central Institute of Engineering, Electronics and Analytics - Electronic Systems, Forschungszentrum Jülich, Jülich, Germany

[9]Alfred Wegener Institute, Helmholtz Center for Polar and Marine

28 Research, Potsdam, Germany

**The rise of ammonia emissions in Asia is predicted to increase radiative cooling and air pollution by forming ammonium nitrate particles in the lower troposphere. There is, however, a severe lack of knowledge about ammonia and ammoniated aerosol particles in the upper troposphere and their possible effects on the formation of clouds. Here we employ satellite observations and high-altitude aircraft measurements, combined with atmospheric trajectory simulations and cloud-chamber experiments, to demonstrate the presence of ammonium nitrate particles and also track the source of ammonia forming into the particles. We find that solid ammonium nitrate particles are surprisingly ubiquitous in the upper troposphere from the Eastern Mediterranean to the Western Pacific during the Asian monsoon period – even as early as 1997. We show that this ammonium nitrate aerosol layer is fed by convection that transports large amounts of ammonia from surface sources into the upper troposphere. Impurities of ammonium sulfate allow for the crystallization of ammonium nitrate even at conditions of high relative humidity prevailing in the upper troposphere. Solid ammonium nitrate particles in the upper troposphere play a hitherto neglected role in ice cloud formation and the aerosol indirect radiative forcing.**

Particulate ammonium nitrate (AN, $NH_4NO_3$) and ammonium sulfate (AS, $(NH_4)_2SO_4$) are important species in the tropospheric aerosol system. Ammonia ($NH_3$), as the most abundant alkaline gas in the atmosphere, is the major precursor for the formation of these aerosols [1, 2]. Emissions of $NH_3$ are estimated to keep rising over the coming decades [3, 4, 5, 6]. Model calculations indicate that this will lead to an increase of the reflected solar radiation through AN particles, mainly produced in the lower part of the troposphere [7, 8]. At upper tropospheric levels, the presence of $NH_3$ may strongly enhance new particle formation through stabilization of sulfuric acid clusters especially at low temperatures prevalent at altitudes near the tropopause [9, 10]. Also in the upper troposphere (UT), solid AS particles were identified as potential ice nucleating particles affecting the formation and radiative properties of cirrus clouds [11]. Yet solid AS, as well as AN particles remain unobserved on a global scale in the UT. Furthermore, AN is generally assumed to exist as aqueous solution under UT conditions, so that it cannot promote heterogeneous ice formation [12, 13].

The presence of $NH_3$ in the UT has recently been revealed by satellite observations during the Asian monsoon [14]. During that season, polluted air masses transported convectively from the boundary layer to high altitudes are confined in the so-called Asian summer Monsoon Anticyclone (AMA), e.g. [15]. In the AMA, pollution accumulates and is dispersed over a large area of the northern hemisphere reaching longitudes of 10–140°E and latitudes from 10–40°N [16, 17, 18, 19, 20, 21]. Air, which is exported from the AMA, influences the composition of the entire northern hemisphere lowermost stratosphere in summer [22, 23].

Connected to the AMA, a layer of enhanced aerosol loading at altitudes of 14–18 km was observed by satellite [24, 25, 26], and balloon-borne instruments [27]. Although little is known about the composition of the aerosol particles forming this Asian Tropopause Aerosol Layer (ATAL), its particles are currently believed to consist of carbonaceous and sulfate material and mineral dust [28, 29, 30, 31] or nitrate [32]. The ATAL particles are often connected with the presence of pollution markers in the monsoon circulation and large $SO_2$ emissions in South East Asia [26, 27]. Observations of the composition of ATAL aerosol particles are, however, sparse. Preliminary data from two single balloon flights indicate a presence of nitrate aerosol particles [27].

## Solid AN discovered by satellite and laboratory measurements

The first evidence of solid AN aerosol particles in the UT is provided by satellite observations with the CRISTA (CRyogenic Infrared Spectrometers and Telescopes for the Atmosphere) instrument inside the AMA in August 1997. We identified a distinct spectral signature at $831\,cm^{-1}$ that is only present in spectra taken inside the AMA as the $\nu_2(NO_3^-)$ band of solid AN (Methods, Supplementary Fig. 1) [33]. Neither aqueous AN, nor any other aerosol or trace gas could replicate the observed spectral feature.

We investigated the crystallization behaviour of aqueous AN aerosol particles at temperature conditions of the UT by AIDA (Aerosol Interaction and

Dynamics in the Atmosphere) aerosol and cloud chamber measurements. In agreement with previous studies that extended down to a temperature of -35°C [12], we did not detect the efflorescence of pure aqueous AN aerosol particles. However, the formation of solid AN was observed for particles composed of aqueous mixtures of AN and AS. At -50°C, already a mole fraction of 2.9 mol% AS was sufficient to initiate the crystallization of AN. The crystallization rate was dependent on the ambient relative humidity (RH) with respect to supercooled liquid water. On a timescale of several hours, the formation of solid AN particles was even observed at RHs as high as 61%, corresponding to an almost ice-saturated environment at -50°C (Methods and Supplementary Information). By demonstrating that small amounts of sulfate facilitate the formation of solid AN even at high RH, these experimental results strongly support the satellite detection of solid AN particles within the AMA. Further, the highly resolved laboratory infrared spectra of the $\nu_2(NO_3^-)$ absorption band at low temperature provide the basis for a quantitative retrieval of AN particle mass density distributions from satellite and airborne observations (Methods).

The spatially resolved AN observations with the CRISTA satellite reveal that enhanced concentrations of AN (0.05–0.3 $\mu g\,m^{-3}$) are located only within the AMA (Fig. 1). These observations between 8 and 16 August 1997 indicate that an ATAL was present in the Asian monsoon UT in summer 1997, years earlier than hitherto thought [25].

The seasonal and inter-annual variability of AN concentrations in the AMA between 2002 and 2011 has been derived by analysis of spaceborne MIPAS (Michelson Interferometer for Passive Atmospheric Sounding) ob-

servations (Methods). Enhanced levels of AN appear in the second half of June, increase in areal coverage and concentration until mid-end of August, and reach values comparable to those derived from the CRISTA instrument (Fig. 2a). During these periods, the maximum concentrations are always located within the confines of the AMA, e.g. reaching as far as the Eastern Mediterranean (Supplementary Figs. 5, 6). This seasonal cycle is modulated by a large inter-annual variability with a clear maximum in 2008 with values three to four times higher than during other years.

Simultaneously observed concentrations of $NH_3$ from a new MIPAS dataset (Methods) start to increase by mid-end of June, reach a maximum by mid-end of July and vanish until end of August (Fig. 2b and Supplementary Figs. 5, 6). This temporal evolution indicates a delay of 1–2 weeks of the AN maximum with respect to $NH_3$. This is consistent with the notion of advective upward transport in the monsoon anticyclone at potential temperatures above about 360 K, which is much slower than convection [34]. In spite of this delay, the onset of enhanced values of AN and $NH_3$ inside the AMA appears simultaneously by end of June.

# AN particles observed from aircraft in upper troposphere

High-altitude aircraft flights from Kathmandu, Nepal in July and August 2017 within the StratoClim project (`http://www.stratoclim.org/`) provided the first opportunity to measure the distribution and composition of

aerosols and trace gases inside the Asian monsoon UT with a variety of in situ and remote sounding instruments. Altitude profiles of AN and $NH_3$ along the flight track with a greatly improved resolution compared to the satellite products have been obtained from infrared limb-imaging observations with the airborne GLORIA (Gimballed Limb Observer for Radiance Imaging of the Atmosphere) instrument (Methods) [35, 36]. Figure 3 presents cross-sections of AN and $NH_3$ along the flight track on 31 July 2017 leading from Kathmandu (27.7°N, 85.4°E) southwest-bound to about 21°N, 79°E and back. Due to the limb-sounding instrument's observational direction to the right of the aircraft, the GLORIA measurements sampled air-masses of different origin during the SW-bound and NE-bound flight legs. During the SW-bound flight leg, we observed enhanced concentrations of AN aerosol mass reaching up to $0.7\,\mu g\,m^{-3}$ at around 16–17 km altitude (Fig. 3a,b). The height of this layer coincides with the typical altitude of the ATAL [26] and with our satellite retrievals. During the first part of the flight, a lower region of enhanced AN concentrations of up to $0.5\,\mu g\,m^{-3}$ between 12 km and 15 km altitude has been observed.

Distinct layers of enhanced values of total aerosol volume density are also observed by in-situ particle size distribution measurements during the ascent and descent of the aircraft on 31 July 2017 (Fig. 4a) [37, 38] (Methods). These correlate very well with maxima in the nitrate mass concentration profiles as measured by a flash vaporization/continuous ionization aerosol mass spectrometer (ERICA-AMS) [39, 40, 41] (Methods) (Fig. 4b). Though there is no exact coincidence between remote sensing and in situ measurements, the aerosol layer in the upper part of the profiles above about 15 km

is present in both kind of observations, as well as a second layer below. The retrieved values of nitrate aerosol mass concentration of around $0.3\,\mu g\,m^{-3}$ from the infrared sounder fit to the independent in situ observations by the mass spectrometer (Supplementary Fig. 7).

Assuming the particle mass density of AN ($1.72\,g\,cm^{-3}$) for conversion of the observed aerosol volume densities to $NO_3^-$ mass concentrations, the resulting maximum values at 13–14 and 16 km agree with the mass spectrometric data within the error margins. Thus, the hypothesis that a major fraction of the ATAL particle mass consists of AN is consistent with the observed aerosol volume densities at peak $NO_3^-$ mass concentrations.

Additionally, the aerosol mass spectrometer detected the simultaneous presence of sulfate and nitrate in the mass spectra of individual single particles (Methods, Supplementary Fig. 9). Such common occurrence of both components was observed in more than 91% of the particles analysed between 10 and 17 km during the flight of 31 July 2017. These findings corroborate the results from the cloud-chamber observations on the crystallization behaviour of aqueous AS/AN mixtures.

## Ground $NH_3$ as the source of upper tropospheric AN particles

The region of enhanced AN at 12–15 km altitude during the first part of the flight (Fig. 3a, b) frames a zone of maximum concentrations of $NH_3$ (Fig. 3c, d). In this region, $NH_3$ volume mixing ratios reach values of 1 ppbv

at 13.5 km altitude. During the previous flight, on 29 July 2017, $NH_3$ mixing ratios of even 1.4 ppbv have been encountered at similar altitudes. These concentrations are up to 40 times higher than the values reported previously [14], and are, thus, by far the highest concentrations of $NH_3$ ever observed in the UT.

High AN mass concentrations observed closely to the region of enhanced mixing ratios of $NH_3$ might either be due to similar source regions or by newly formed AN particles through gas to particle conversion within the plume of elevated $NH_3$ concentrations. Conversion of $NH_3$ volume mixing ratios to equivalent AN mass concentrations leads to maximum values of up to $1\,\mu g\,m^{-3}$. Thus, the GLORIA measurements of that particular day show sufficiently high values of the gas phase $NH_3$ mixing ratios to explain concentrations up to $0.7\,\mu g\,m^{-3}$ of AN.

We have studied the possible origin of the elevated $NH_3$ concentrations in the UT by trajectory analyses in combination with satellite data of total column amounts of $NH_3$ [42] (Methods, Supplementary Figs. 10 and 11). During the days prior to our aircraft measurements, enhanced column amounts of $NH_3$ have been observed at lower atmospheric levels in the region of NW-India and NE-Pakistan, a region known as a hot-spot for $NH_3$ emissions [6, 43, 44]. Trajectory simulations suggest that the high amounts of $NH_3$ observed by the GLORIA instrument have initially been transported convectively to altitudes of 12–14 km. Subsequently, they were advected by the anticyclonic upper tropospheric monsoon circulation to the location of the airborne observations within a few days. These measurements prove that $NH_3$ reaches the UT in amounts sufficient to explain the mass density of AN

observed. The relevant processes reducing the impact of washout of $NH_3$ during convection might involve low acidity of convective rain droplets [45], or a release of $NH_3$ during the freezing process of cloud particles [46, 47, 48].

We uncover that a considerable part of the aerosol particles in the AMA consists of solid AN being formed through convective uplift of $NH_3$ from intense surface emissions. Due to its longer lifetime, AN is subsequently transported vertically and horizontally inside the AMA, thereby already influencing a large area of the northern hemisphere. Air masses with enhanced AN are not confined within the AMA but are transported either into the lowermost stratosphere at mid-latitudes or into the tropical belt. Here, due to dilution, the AN concentrations are no longer visible in our satellite data. It is highly probable that in the UT, these solid particles act as effective ice nucleating particles as has previously been demonstrated for solid AS [11].

In the future, rising emissions of $NH_3$ will probably lead to a change of AN particles also in the UT with potential consequences for the Earth's radiative budget. For quantitative assessments using chemical-dynamical models, a better quantification of the $NH_3$ surface emissions over the Indian sub-continent as well as a deeper understanding of the interaction processes of $NH_3$ with liquid water and ice during convection is needed. Furthermore, it is most important to characterize the ice nucleating capacity of solid AN particles.

# Methods

## Cloud chamber observations

The AIDA aerosol and cloud chamber is a highly instrumented, 84.5 $m^3$-sized aluminium vessel that can be operated at temperatures between +60 and -90°C [49]. The ambient relative humidity can be controlled by evaporating a specified amount of water vapour into the chamber. The number concentration and size distribution of aerosol particles added to the chamber are measured with a condensation particle counter (CPC, model 3010, TSI), a scanning mobility particle sizer (SMPS, model 3071A, TSI), and an aerodynamic particle spectrometer (APS, model 3321, TSI). Relative humidity is measured in situ by tunable diode laser (TDL) absorption spectroscopy, detecting a rotational-vibrational water vapour absorption line at 1.37 $\mu$m [50]. Infrared extinction spectra of the aerosol particles are recorded in situ with a FTIR spectrometer (model IFS66v, Bruker) coupled to a multiple reflection cell (optical path length 166.8 m, wavenumber range 6000–800 $cm^{-1}$, 0.5 $cm^{-1}$ resolution) [51]. With polarization-resolved in situ laser light scattering measurements, the backscattering linear depolarization ratio of the aerosol particles at a scattering angle of 178° and a wavelength of 488 nm are determined [52]. Due to the different infrared spectral signatures of liquid and solid AN, as well as the different depolarization levels of spherical, aqueous AN solution droplets and aspherical, crystalline AN particles, both the infrared and depolarization measurements allow for studying the phase change behaviour of the added aerosol particles. A schematic of the AIDA facility and further details about its optical instrumentation can be found in

[53].

For our experiments, the AIDA chamber was held at -50°C and two different relative humidities with respect to supercooled water, i.e., at 22% and 61% RH, in order to simulate dry and humid upper tropospheric air masses. The aerosol particles were generated from aqueous solutions of 100 mol% AN, 90 mol% AN + 10 mol% AS, and 97.1 mol% AN + 2.9 mol% AS. The bulk solutions were prepared by dissolving the respective chemicals (AN, VWR Chemicals, 99%; AS, Merck, 99.5%) in high purity water (GenPure Pro UV ultrapure water system, Thermo Scientific), using an overall solute concentration of 10 wt%. Aqueous solution droplets were produced with an ultrasonic nebulizer (GA 2400, SinapTec). The aerosol flow first passed a set of silica gel diffusion dryers (Topas GmbH) to reduce the RH in the aerosol flow to $\leq 3\%$ and was then injected into the AIDA chamber through a stainless steel tube. The spectrum of liquid AN shown in Supplementary Fig. 1 was recorded after injection of the 100 mol% AN solution into the AIDA chamber at 61% RH, whereas the spectrum of the crystalline phase was recorded for the 97.1 mol% AN + 2.9 mol% AS mixture at 22% RH. Pertinent details of these experiments are further discussed in the Supplementary Information.

In order to derive mass-specific absorption coefficients of the recorded $\nu_2(NO_3^-)$ infrared absorption band of crystalline AN (Supplementary Fig. 1), which were then used as input for the aerosol mass density retrievals from the satellite observations, we computed the total mass concentration of the aerosol particles suspended in the AIDA chamber. In the first step, the volume size distribution of the aerosol particles was computed from the combination of the SMPS and APS size spectra, employing a particle density

of $1.72\,\mathrm{g\,cm^{-3}}$ and a dynamic shape factor of 1.1 to convert the mobility and aerodynamic diameters from the SMPS and APS measurements into the equal-volume sphere diameter (Supplementary Fig. 3). The integrated volume concentration was then multiplied with the particle density to yield the total mass concentration of the crystallized particle ensemble. Finally, the smaller mass fraction of AS, which does not contribute to the signature of the $\nu_2(NO_3^-)$ absorption band at $831\,\mathrm{cm^{-1}}$, was subtracted to yield the mass concentration of AN only. The uncertainty for the AN mass density, mainly arising from the uncertainties associated with the employed values for the particle density and the dynamic shape factor, was estimated to $\pm 30\%$.

## Remote sensors

CRISTA: The Space Shuttle experiment CRISTA (CRyogenic Infrared Spectrometers and Telescopes for the Atmosphere) was flown on the Shuttle Pallet Satellite in November 1994 (STS 66) and August 1997 (STS 85) [54, 55, 56]. The instrument was equipped with three optical telescopes and four spectrometers covering spectral ranges from 140 to $2500\,\mathrm{cm^{-1}}$ using 26 detectors. The spectral resolution was $\lambda/\Delta\lambda \approx 500$, with wavelength $\lambda$. In the spectral range around $800\,\mathrm{cm^{-1}}$, this corresponds to a resolution of $\approx 1.5\,\mathrm{cm^{-1}}$. During CRISTA-2 (STS85) the main measurement mode covered tangent heights from 11 to 75 km with a vertical sampling step of 2 km and a vertical field of view width of about 1.5 km. The horizontal sampling pattern of this mode was 200 km along track and 650 km across track.

MIPAS: The limb-sounder MIPAS (Michelson Interferometer for Passive

Atmospheric Sounding) was in operation between 2002 and 2012 on board the polar orbiting satellite Envisat [57]. It recorded atmospheric emission spectra in the thermal infrared region between 685 and 2410 $\mathrm{cm}^{-1}$ with spectral resolutions of 0.025 $\mathrm{cm}^{-1}$ in the first measurement period from July 2002 to March 2004 and 0.0625 $\mathrm{cm}^{-1}$ during the second period from January 2005 to April 2012. In nominal rearward viewing limb-scan mode, tangent altitudes covered regions between 7 and 72 km with a vertical sampling of 3 km up to 42 km in the period 2002–2004 and 1.5 km up to 22 km altitude during 2005–2012, respectively. The along-track sampling distance between limb-scans was 550 km during the first and 420 km during the second measurement period. Retrievals are performed on basis of level-1B calibrated radiances version 5.02/5.06 provided by ESA.

GLORIA: The airborne limb-imaging spectrometer GLORIA (Gimballed Limb Observer for Radiance Imaging of the Atmosphere) covers the mid-infrared spectral range from 780 to 1400 $\mathrm{cm}^{-1}$ [35, 36]. During the StratoClim monsoon campaign, GLORIA was deployed on the Geophysica high-altitude aircraft performing limb observations with an azimuth of 90° to the right hand side. Geophysica is a Russian high-altitude aircraft of the type M55, built and operated by Myasishchev Design Bureau, Zhukovsky, Moscow Region. GLORIA takes one limb-image of 128 vertical × 48 horizontal pixels with a spectral resolution of 0.0625 $\mathrm{cm}^{-1}$ within 13 s. The vertical elevation coverage is 4.1°. The spectra of horizontal pixel rows are averaged for noise reduction. In combination with the typical velocity of the aircraft of 700 to 750 $\mathrm{km\,h}^{-1}$ this corresponds to an along track sampling of around 3 km. The generation of calibrated spectra from GLORIA observations has been

described in [58].

## Identification and retrieval of ammonium nitrate (AN) from infrared limb observations

In previous infrared limb observations, the infrared $\nu_2$ out-of-plane deformation band of $NO_3^-$ in nitric acid trihydrate (NAT) at 821 $cm^{-1}$ [59, 60, 61] has been used to detect and quantify NAT particles within polar stratospheric clouds [62, 63, 64]. This spectral band is especially suited for detection from limb-viewing sensors since it is located in one of the window regions in the mid-infrared least affected by trace gas signatures. Further, compared to other spectral bands of solids, the nitrate $\nu_2$ band is so sharp that it can easily be identified.

The $\nu_2(NO_3^-)$ - band of ammonium nitrate (AN) has frequently been assigned in laboratory spectra to wavenumbers around 831 $cm^{-1}$: 830 $cm^{-1}$ [65], 831–833 $cm^{-1}$ [66], 830–832 $cm^{-1}$ [60], 831 $cm^{-1}$[33]. The only field observations where the $\nu_2(NO_3^-)$ band was identified in collected samples of ambient aerosols have been reported in [67] and, tentatively, in [68].

Supplementary Figures 1 and 4 show the detection of the $\nu_2(NO_3^-)$ - band of AN in infrared spectra of the spaceborne limb sounding instruments CRISTA and MIPAS, as well as observed by GLORIA during the StratoClim aircraft campaign. From difference spectra of observations at similar tangent altitudes but at different locations, a spectral band with maximum close to 831 $cm^{-1}$ and width of about 3 $cm^{-1}$ could clearly be identified - exactly at the position of the $\nu_2(NO_3^-)$ band of AN. An intensive search for an alternative

explanation of this signature, either by other kinds of aerosol particles or by gas phase species was not successful. For example, AS, ammonium bisulfate $(NH_4)HSO_4$ and letovicite $(NH_4)_3H(SO_4)_2$ do not show any band around $830\,cm^{-1}$ [69, 70] , as well as mineral dust [71] and dicarboxylic acids like oxalic acid ($C_2H_2O_4$), malonic acid ($C_3H_4O_4$) [72] or succinic acid ($C_4H_6O_4$) [73]. Apart from NAT and AN, other nitrates, do show the sharp peak of the $\nu_2(NO_3^-)$-band in the 820-840 $cm^{-1}$ region of the infrared spectrum, however, not at the position of AN, e.g. sodium nitrate ($NaNO_3$) at $836\,cm^{-1}$ [74, 75], or potassium nitrate ($KNO_3$) at $825\,cm^{-1}$ [74].

As shown in our AIDA measurements as well as in [33], an aqueous solution of AN also has a spectral signature in that spectral region (Supplementary Fig. 3). However, it is clearly distinct from the solid AN peak since its maximum is located at $829\,cm^{-1}$ and its width is about twice the width of the solid AN signature. Thus, it does not fit to our observed spectra (Supplementary Figs. 1 and 4). We, therefore, conclude that the spectral signature consistently observed inside the AMA by the three different instruments is caused by aerosol composed of AN in solid state.

The absorption coefficients as derived from the aerosol chamber experiments have been used for the retrieval of vertical profiles of AN mass density from observations of CRISTA, MIPAS and GLORIA. In case of MIPAS and GLORIA the same processing scheme as used for $NH_3$ (see below) has been applied. For analysis of CRISTA observations, the retrieval employs the processing scheme of the airborne successor instrument already used for deriving PAN in the AMA [76, 19]; the measurement density was improved by synoptically interpolating the measurements of five measurement days to a single

point of time in the middle by using trajectory calculations. The spectral window between 828 $cm^{-1}$ and 835 $cm^{-1}$ has been commonly evaluated. Uncertainties for AN mass concentrations are estimated to $\pm 0.03\,\mu g\,m^{-3}$ (single profile precision) ±10% (systematic instrumental/retrieval) ±30% (spectroscopic AN absorption coefficients from the AIDA observations) for GLORIA, ±15% (single profile precision) ±15% (systematic instrumental/retrieval) ±30% (spectroscopy AN) for CRISTA, and, $\pm 0.015\,\mu g\,m^{-3}$ (single profile precision) ±30%$\pm 0.01\,\mu g\,m^{-3}$ (systematic instrumental/retrieval) ±30% (spectroscopy AN) in case of MIPAS. The values of vertical resolutions are 0.8 km for GLORIA, 2.2 km for CRISTA, and 4.5 km/3.5 km for the retrieval from the MIPAS observational period 1 and 2, respectively.

## Identification and retrieval of ammonia ($NH_3$) from infrared limb observations

Passive remote sounding is especially suited for detection of $NH_3$ since it avoids problems connected to wall-effects [77, 78]. Retrievals of ammonia vertical volume mixing ratio profiles from MIPAS mean radiance spectra which were averaged over three months and 10° latitude × 10° longitude have been published in [14]. In order to obtain better resolution in time and space, here we have performed retrievals of $NH_3$ from single MIPAS limb-scans. The profile retrievals have been performed as described in [14]. The inversion scheme is a nonlinear least squares fitting in a global-fit approach on 1 km spaced altitude levels [79] regularized by a first-order smoothing operator [80]. The selected spectral windows with $NH_3$ signatures are 965.1–965.6 $cm^{-1}$

and 966.6–967.5 $cm^{-1}$ for the first MIPAS period 965.125–965.625 $cm^{-1}$, and 966.625–967.5 $cm^{-1}$ for the second period. Resulting profiles of $NH_3$ volume mixing ratio are characterized by a vertical resolution of 4–4.5 km/3.5-4 km (1st/2nd period). Uncertainties are estimated according to [14] to ±5 pptv (single profile precision) and ±15% (accuracy).

As in the case of MIPAS, inversion of vertical profiles of $NH_3$ volume mixing ratios from GLORIA calibrated limb-radiances has been performed by application of a constrained nonlinear least-squares fitting scheme, whereby measurements from all infrared spectra of one GLORIA image are used [81, 82]. The retrievals employ an altitude grid spacing of 0.25 km. For the spectral fit, the same spectral windows and inversion procedure as in the case of the MIPAS second measurement period have been used (see above). Supplementary Fig. 8 shows the spectral evidence for $NH_3$ from GLORIA observations taken at a tangent altitude of 13.7 km during the flight on 31 July 2017 at 4:14 UTC where the retrieval resulted in a value of 920 pptv at the 13.75 km altitude level. Here the spectral emission lines of $NH_3$ are clearly identified by comparing the simulations including $NH_3$ to the simulations without consideration of $NH_3$. This proves unambiguously the presence of $NH_3$ with concentrations near 1 ppbv in the UT. The vertical resolution of retrieved profiles is about 0.8 km. The vmr profile uncertainties are estimated based on various parameter uncertainties as described in [81, 82]. They amount to ±8 pptv (single profile precision) ±20% (accuracy).

## In situ sensors on board the Geophysica

ERICA (ERc Instrument for the chemical Composition of Aerosols): The mass spectrometer ERICA is a newly developed in situ instrument combining a laser ablation aerosol mass spectrometer (ERICA-LAMS) similar to [83, 84] with a flash vaporization/electron impact ionization mass spectrometer (ERICA-AMS) based on the Aerodyne Aerosol Mass Spectrometer (AMS) principle [39]. For a quantitative comparison of the aerosol chemical composition, mostly data from the AMS component of ERICA was considered in this study. Here small ensembles of the sampled aerosol particles with size diameters between 60 nm and approximately 2 $\mu$m are vaporized at 600°C followed by electron impact ionization of the vapour [39]. The positive ions are detected by a Time-Of-Flight Mass Spectrometer (TOFMS) from which the particle chemical composition can be inferred [40]. While the reproducibility in the laboratory is better than 5% from calibration to calibration, the uncertainty for the aircraft deployment is estimated to ±30%. Single particle aerosol composition was determined by the LAMS component of ERICA covering a size range from 150 nm to 2 $\mu$m. For each ablated and analysed aerosol particle, the positive and negative ion mass spectra are concurrently recorded by two TOFMSs. This way it is possible to unambiguously identify individual particles which contain both sulfate and nitrate, as can be seen from the example mass spectra in Supplementary Fig. 9. The ERICA-LAMS and ERICA-AMS instrument combination itself and the corresponding sampling inlet system were custom designed similar to [41] for operation on the high altitude research aircraft Geophysica.

UHSAS/COPAS: The ambient aerosol volume density was obtained from particle size distribution measurements by means of an in-house modified UHSAS optical particle counter [37] (mounted underneath the aircraft's wing) and the high-altitude COPAS condensation particle counter [38]. The UHSAS covers a particle size diameter range from 65 nm to 1 $\mu$m and has been modified for operation under stratospheric conditions. One more size bin extending from 10 nm to 65 nm was derived as composite from the COPAS and the UHSAS data.

MAS: The Multiwavelength Aerosol Scatterometer obtained in situ measurements of the aerosol backscatter ratio at 532 nm [85].

## Trajectory calculations

Two different models for estimation of convective events along backward trajectories starting at the GLORIA measurement locations have been used, TRACZILLA and ATLAS.

The TRACZILLA diffusive back-trajectories [86] have been calculated based on ERA5 reanalysis data ($0.25° \times 0.25°$ horizontal resolution, 137 vertical levels, hourly temporal resolution) using kinematic vertical winds. Clusters of 1000 parcels are released along each tangent point with a time resolution of 1 hour. The probability of convective influence along the trajectories is estimated from the high-frequency MSG1 and Himawari geostationary satellites observations of Brightness Temperature (BT). Both satellite images are used, jointed at 90°E longitude, to cover the whole AMA region extent. The trajectory is assumed to encounter a convective event when advected below

a deep convective cloud, the top pressure of which is estimated from the BT, following the same approach as presented in [87].

Trajectories from the ATLAS model [88] are driven by ECMWF ERA Interim reanalysis data ($0.75° \times 0.75°$ horizontal resolution, 6 h temporal resolution) and use a log-pressure coordinate (kinematic trajectories). The trajectory model includes a detailed stochastic parameterization of convective transport driven by ERA Interim convective mass fluxes and detrainment rates. At every measurement location of GLORIA, 1000 backward ensemble trajectories are started, which take different paths due to the stochastic nature of the convective transport scheme.

Supplementary Figs. 10 and 11 show backward trajectories starting at the GLORIA measurement locations on 31 Jul 2017 calculated by TRACZILLA and ATLAS, respectively. For the SW-bound flight leg, exemplary 30 day non-convective backward trajectories are shown, starting at locations with an $NH_3$ concentrations enhancement larger than 0.4 ppbv. For the NE-bound leg, exemplary trajectories starting in the same altitude range (12–14 km) are shown for comparison. The trajectories show that the history of the airmasses corresponding to enhanced $NH_3$ concentrations is different from the one where no $NH_3$ has been detected. Further, consistently in both models, maxima in the convective event density along the trajectories with enhanced $NH_3$, as indicated by white contour lines, are located over the Himalayas and the Tibetan plateau as well as over NW-India and NE-Pakistan. The latter region is clearly correlated with a region of high column amounts as observed by the IASI satellite instruments during the days before the aircraft observations. Thus, we conclude that it is very likely that the high $NH_3$

499 concentrations observed by GLORIA have been injected into the UT over
500 NW-India and NE-Pakistan by strong convection in a region where, near the
501 ground, high $NH_3$ concentrations are prevalent.

# References


[1] Dentener, F. J. & Crutzen, P. J. A three-dimensional model of the global ammonia cycle. *J. Atmos. Chem.* **19**, 331–369 (1994). URL https://doi.org/10.1007/BF00694492.

[2] Behera, S. N., Sharma, M., Aneja, V. P. & Balasubramanian, R. Ammonia in the atmosphere: a review on emission sources, atmospheric chemistry and deposition on terrestrial bodies. *Environ. Sci. Pollut. Res.* **20**, 8092–8131 (2013). URL https://doi.org/10.1007/s11356-013-2051-9.

[3] Bouwman, A. *et al.* A global high-resolution emission inventory for ammonia. *Glob. Biogeochem. Cycles* **11**, 561–587 (1997). URL https://doi.org/10.1029/97GB02266.

[4] Erisman, J. W., Sutton, M. A., Galloway, J., Klimont, Z. & Winiwarter, W. How a century of ammonia synthesis changed the world. *Nature Geosci.* **1**, 636–639 (2008). URL https://doi.org/10.1038/ngeo325.

[5] Warner, J. X. *et al.* Increased atmospheric ammonia over the world's major agricultural areas detected from space. *Geophys. Res. Lett.* **44**, 2875–2884 (2017). URL https://doi.org/10.1002/2016GL072305.

[6] Xu, R. T. *et al.* Half-century ammonia emissions from agricultural systems in southern Asia: Magnitude, spatiotemporal patterns, and implications for human health. *Geohealth* **2**, 40–53 (2018). URL https://doi.org/10.1002/2017GH000098.

[7] Hauglustaine, D. A., Balkanski, Y. & Schulz, M. A global model simulation of present and future nitrate aerosols and their direct radiative forcing of climate. *Atmos. Chem. Phys.* **14**, 11031–11063 (2014). URL https://doi.org/10.5194/acp-14-11031-2014.

[8] IPCC. *Climate Change 2013: The Physical Science Basis. Contribution of Working Group I to the Fifth Assessment Report of the Intergovernmental Panel on Climate Change* (Cambridge University Press, Cambridge, United Kingdom and New York, NY, USA, 2013). URL www.climatechange2013.org.

[9] Kirkby, J. *et al.* Role of sulphuric acid, ammonia and galactic cosmic rays in atmospheric aerosol nucleation. *Nature* **476**, 429–433 (2011). URL https://doi.org/10.1038/nature10343.

[10] Kürten, A. *et al.* Experimental particle formation rates spanning tropospheric sulfuric acid and ammonia abundances, ion production rates, and temperatures. *J. Geophys. Res.* **121**, 12,377–12,400 (2016). URL https://doi.org/10.1002/2015JD023908.

[11] Abbatt, J. P. D. *et al.* Solid ammonium sulfate aerosols as ice nuclei: A pathway for cirrus cloud formation. *Science* (2006). URL https://doi.org/10.1126/science.1129726.

[12] Cziczo, D. J. & Abbatt, J. P. D. Infrared observations of the response of NaCl, $MgCl_2$, $NH_4HSO_4$, and $NH_4NO_3$ aerosols to changes in relative humidity from 298 to 238 K. *J. Phys. Chem. A* **104**, 2038–2047 (2000). URL https://doi.org/10.1021/jp9931408.

[13] Cziczo, D. J. & Abbatt, J. P. D. Ice nucleation in $NH_4HSO_4$, $NH_4NO_3$, and $H_2SO_4$ aqueous particles: Implications for cirrus cloud formation. *Geophys. Res. Lett.* **28**, 963–966 (2001). URL https://doi.org/10.1029/2000GL012568.

[14] Höpfner, M. *et al.* First detection of ammonia ($NH_3$) in the Asian summer monsoon upper troposphere. *Atmos. Chem. Phys.* **16**, 14357–14369 (2016). URL https://doi.org/10.5194/acp-16-14357-2016.

[15] Ploeger, F. *et al.* A potential vorticity-based determination of the transport barrier in the Asian summer monsoon anticyclone. *Atmos. Chem. Phys.* **15**, 13145–13159 (2015). URL https://doi.org/10.5194/acp-15-13145-2015.

[16] Park, M., Randel, W. J., Gettelman, A., Massie, S. T. & Jiang, J. H. Transport above the Asian summer monsoon anticyclone inferred from Aura Microwave Limb Sounder tracers. *J. Geophys. Res.* **112**, 253 (2007). URL https://doi.org/10.1029/2006JD008294.

[17] Park, M. *et al.* Chemical isolation in the Asian monsoon anticyclone observed in Atmospheric Chemistry Experiment (ACE-FTS) data. *Atmos. Chem. Phys.* **8**, 757–764 (2008). URL https://doi.org/10.5194/acp-8-757-2008.

[18] Randel, W. J. *et al.* Asian monsoon transport of pollution to the stratosphere. *Science* **328**, 611–613 (2010). URL https://doi.org/10.1126/science.1182274.

[19] Ungermann, J. *et al.* Observations of PAN and its confinement in the Asian summer monsoon anticyclone in high spatial resolution. *Atmos. Chem. Phys.* **16**, 8389–8403 (2016). URL https://doi.org/10.5194/acp-16-8389-2016.

[20] Santee, M. L. *et al.* A comprehensive overview of the climatological composition of the Asian summer monsoon anticyclone based on 10 years of Aura Microwave Limb Sounder measurements. *J. Geophys. Res.* **122**, 5491–5514 (2017). URL https://doi.org/10.1002/2016JD026408.

[21] Lelieveld, J. *et al.* The South Asian monsoon: Pollution pump and purifier. *Science* (2018). URL https://doi.org/10.1126/science.aar2501.

[22] Ploeger, F., Konopka, P., Walker, K. & Riese, M. Quantifying pollution transport from the Asian monsoon anticyclone into the lower stratosphere. *Atmos. Chem. Phys.* **17**, 7055–7066 (2017). URL https://doi.org/10.5194/acp-17-7055-2017.

[23] Yu, P. *et al.* Efficient transport of tropospheric aerosol into the stratosphere via the Asian summer monsoon anticyclone. *Proc. Natl. Acad. Sci. U.S.A.* **114**, 6972–6977 (2017). URL https://doi.org/10.1073/pnas.1701170114.

[24] Vernier, J.-P., Thomason, L. W. & Kar, J. CALIPSO detection of an Asian tropopause aerosol layer. *Geophys. Res. Lett.* **38** (2011). URL https://doi.org/10.1029/2010GL046614.

[25] Thomason, L. W. & Vernier, J.-P. Improved SAGE II cloud/aerosol categorization and observations of the Asian tropopause aerosol layer: 1989-2005. *Atmos. Chem. Phys.* **13**, 4605–4616 (2013). URL https://doi.org/10.5194/acp-13-4605-2013.

[26] Vernier, J. P. *et al.* Increase in upper tropospheric and lower stratospheric aerosol levels and its potential connection with Asian pollution. *J. Geophys. Res.* **120**, 1608–1619 (2015). URL https://doi.org/10.1002/2014JD022372.

[27] Vernier, J.-P. *et al.* BATAL: The balloon measurement campaigns of the Asian tropopause aerosol layer. *Bull. Amer. Met. Soc.* **99**, 955–973 (2018). URL https://doi.org/10.1175/BAMS-D-17-0014.1.

[28] Fadnavis, S. *et al.* Transport of aerosols into the UTLS and their impact on the Asian monsoon region as seen in a global model simulation. *Atmos. Chem. Phys.* **13**, 8771–8786 (2013). URL https://doi.org/10.5194/acp-13-8771-2013.

[29] Neely, R. R. *et al.* The contribution of anthropogenic $SO_2$ emissions to the Asian tropopause aerosol layer. *J. Geophys. Res.* **119**, 1571–1579 (2014). URL https://doi.org/10.1002/2013JD020578.

[30] Yu, P., Toon, O. B., Neely, R. R., Martinsson, B. G. & Brenninkmeijer, C. A. M. Composition and physical properties of the Asian tropopause aerosol layer and the North American tropospheric aerosol layer. *Geophys. Res. Lett.* **42**, 2540–2546 (2015). URL https://doi.org/10.1002/2015GL063181.

[31] Lau, W. K. M., Yuan, C. & Li, Z. Origin, maintenance and variability of the Asian Tropopause Aerosol Layer (ATAL): The roles of monsoon dynamics. *Sci. Rep.* **8**, 3960 (2018). URL https://doi.org/10.1038/s41598-018-22267-z.

[32] Gu, Y., Liao, H. & Bian, J. Summertime nitrate aerosol in the upper troposphere and lower stratosphere over the Tibetan Plateau and the South Asian summer monsoon region. *Atmos. Chem. Phys.* **16**, 6641–6663 (2016). URL https://www.atmos-chem-phys.net/16/6641/2016/.

[33] Schlenker, J. C. & Martin, S. T. Crystallization pathways of sulfate-nitrate-ammonium aerosol particles. *J. Phys. Chem. A* **109**, 9980–9985 (2005). URL https://doi.org/10.1021/jp052973x.

[34] Vogel, B. *et al.* Lagrangian simulations of the transport of young air masses to the top of the Asian monsoon anticyclone and into the tropical pipe. *Atmos. Chem. Phys. Discuss.* **2018**, 1–38 (2018). URL https://doi.org/10.5194/acp-2018-724.

[35] Friedl-Vallon, F. *et al.* Instrument concept of the imaging Fourier transform spectrometer GLORIA. *Atmos. Meas. Tech.* **7**, 3565–3577 (2014). URL https://doi.org/10.5194/amt-7-3565-2014.

[36] Riese, M. *et al.* Gimballed Limb Observer for Radiance Imaging of the Atmosphere (GLORIA) scientific objectives. *Atmos. Meas. Tech.* **7**, 1915–1928 (2014). URL https://doi.org/10.5194/amt-7-1915-2014.

[37] Cai, Y., Montague, D. C., Mooiweer-Bryan, W. & Deshler, T. Performance characteristics of the ultra high sensitivity aerosol spectrometer for particles between 55 and 800 nm: Laboratory and field studies. *J. Aerosol Sci.* **39**, 759 – 769 (2008). URL https://doi.org/10.1016/j.jaerosci.2008.04.007.

[38] Weigel, R. *et al.* In situ observations of new particle formation in the tropical upper troposphere: the role of clouds and the nucleation mechanism. *Atmos. Chem. Phys.* **11**, 9983–10010 (2011). URL https://doi.org/10.5194/acp-11-9983-2011.

[39] Drewnick, F. *et al.* A new time-of-flight aerosol mass spectrometer (TOF-AMS) - instrument description and first field deployment. *Aerosol Sci. Technol.* **39**, 637–658 (2005). URL https://doi.org/10.1080/02786820500182040.

[40] Allan, J. D. *et al.* A generalised method for the extraction of chemically resolved mass spectra from aerodyne aerosol mass spectrometer data. *J. Aerosol Sci.* **35**, 909 – 922 (2004). URL https://doi.org/10.1016/j.jaerosci.2004.02.007.

[41] Schulz, C. *et al.* Aircraft-based observations of isoprene-epoxydiol-derived secondary organic aerosol (IEPOX-SOA) in the tropical upper troposphere over the Amazon region. *Atmos. Chem. Phys.* **18**, 14979–15001 (2018). URL https://doi.org/10.5194/acp-18-14979-2018.

[42] Van Damme, M. *et al.* Version 2 of the IASI $NH_3$ neural network retrieval algorithm: near-real-time and reanalysed datasets. *Atmos.*

*Meas. Tech.* **10**, 4905–4914 (2017). URL https://doi.org/10.5194/amt-10-4905-2017.

[43] Clarisse, L., Clerbaux, C., Dentener, F., Hurtmans, D. & Coheur, P.-F. Global ammonia distribution derived from infrared satellite observations. *Nature Geosci.* **2**, 479–483 (2009). URL http://dx.doi.org/10.1038/ngeo551.

[44] van Damme, M. *et al.* Industrial and agricultural ammonia point sources exposed. *Nature* **564**, 99 (2018). URL https://doi.org/10.1038/s41586-018-0747-1.

[45] Metzger, S., Dentener, F., Krol, M., Jeuken, A. & Lelieveld, J. Gas/aerosol partitioning 2. Global modeling results. *J. Geophys. Res.* **107**, ACH 17–1–ACH 17–23 (2002). URL https://doi.org/10.1029/2001JD001103.

[46] Hoog, I., Mitra, S. K., Diehl, K. & Borrmann, S. Laboratory studies about the interaction of ammonia with ice crystals at temperatures between 0 and −20°C. *J. Atmos. Chem.* **57**, 73–84 (2007). URL https://doi.org/10.1007/s10874-007-9063-0.

[47] Jost, A., Szakáll, M., Diehl, K., Mitra, S. K. & Borrmann, S. Chemistry of riming: the retention of organic and inorganic atmospheric trace constituents. *Atmos. Chem. Phys.* **17**, 9717–9732 (2017). URL https://doi.org/10.5194/acp-17-9717-2017.

[48] Ge, C., Zhu, C., Francisco, J. S., Zeng, X. C. & Wang, J. A molecular perspective for global modeling of upper atmospheric $NH_3$ from freezing

clouds. *Proc. Natl. Acad. Sci. U.S.A.* (2018). URL https://doi.org/10.1073/pnas.1719949115.

[49] Möhler, O. *et al.* Experimental investigation of homogeneous freezing of sulphuric acid particles in the aerosol chamber AIDA. *Atmos. Chem. Phys.* **3**, 211–223 (2003). URL https://doi.org/10.5194/acp-3-211-2003.

[50] Fahey, D. W. *et al.* The AquaVIT-1 intercomparison of atmospheric water vapor measurement techniques. *Atmos. Meas. Tech.* **7**, 3177–3213 (2014). URL https://doi.org/10.5194/amt-7-3177-2014.

[51] Wagner, R., Benz, S., Möhler, O., Saathoff, H. & Schurath, U. Probing ice clouds by broadband mid-infrared extinction spectroscopy: case studies from ice nucleation experiments in the AIDA aerosol and cloud chamber. *Atmos. Chem. Phys.* **6**, 4775–4800 (2006). URL https://doi.org/10.5194/acp-6-4775-2006.

[52] Schnaiter, M. *et al.* Influence of particle size and shape on the backscattering linear depolarisation ratio of small ice crystals - cloud chamber measurements in the context of contrail and cirrus microphysics. *Atmos. Chem. Phys.* **12**, 10465–10484 (2012). URL https://doi.org/10.5194/acp-12-10465-2012.

[53] Wagner, R. *et al.* A review of optical measurements at the aerosol and cloud chamber AIDA. *J. Quant. Spectrosc. Radiat. Transfer* **110**, 930 – 949 (2009). URL https://doi.org/10.1016/j.jqsrt.2009.01.026.

Light Scattering: Mie and More Commemorating 100 years of Mie's 1908 publication.

[54] Offermann, D. *et al.* Cryogenic Infrared Spectrometers and Telescopes for the Atmosphere (CRISTA) experiment and middle atmosphere variability. *J. Geophys. Res.* **104**, 16311–16325 (1999). URL https://doi.org/10.1029/1998JD100047.

[55] Riese, M. *et al.* Cryogenic Infrared Spectrometers and Telescopes for the Atmosphere (CRISTA) data processing and atmospheric temperature and trace gas retrieval. *J. Geophys. Res.* **104**, 16349–16367 (1999). URL https://doi.org/10.1029/1998JD100057.

[56] Grossmann, K. U. *et al.* The CRISTA-2 mission. *J. Geophys. Res.* **107**, 1–1 (2002). URL https://doi.org/10.1029/2001JD000667.

[57] Fischer, H. *et al.* MIPAS: an instrument for atmospheric and climate research. *Atmos. Chem. Phys.* **8**, 2151–2188 (2008). URL https://doi.org/10.5194/acp-8-2151-2008.

[58] Kleinert, A. *et al.* Level 0 to 1 processing of the imaging Fourier transform spectrometer GLORIA: generation of radiometrically and spectrally calibrated spectra. *Atmos. Meas. Tech.* **7**, 4167–4184 (2014). URL https://doi.org/10.5194/amt-7-4167-2014.

[59] Toon, O. B., Tolbert, M. A., Middlebrook, A. M. & Jordan, J. Infrared optical constants of $H_2O$, ice, amorphous nitric acid solutions, and nitric acid hydrates. *J. Geophys. Res.* **99**, 25631–25654 (1994). URL https://doi.org/10.1029/94JD02388.

[60] Koch, T. G., Holmes, N. S., Roddis, T. B. & Sodeau, J. R. Low-temperature reflection/absorption IR study of thin films of nitric acid hydrates and ammonium nitrate adsorbed on gold foil. *J. Chem. Soc. Faraday Trans.* **92**, 4787 (1996). URL https://doi.org/10.1039/FT9969204787.

[61] Biermann, U. M. *Gefrier- und FTIR-Experimente zur Nukleation und Lebensdauer stratosphärischer Wolken.* Ph.D. thesis, Universität Bielefeld (1998). Cuvillier Verlag, ISBN 3-89712-212-X.

[62] Spang, R. & Remedios, J. J. Observations of a distinctive infra-red spectral feature in the atmospheric spectra of polar stratopsheric clouds measured by the CRISTA instrument. *Geophys. Res. Lett.* **30** (2003). URL https://doi.org/10.1029/2003GL017231.

[63] Höpfner, M. *et al.* Spectroscopic evidence for NAT, STS, and ice in MIPAS infrared limb emission measurements of polar stratospheric clouds. *Atmos. Chem. Phys.* **6**, 1201–1219 (2006). URL https://doi.org/10.5194/acp-6-1201-2006.

[64] Woiwode, W. *et al.* Spectroscopic evidence of large aspherical $\beta$-NAT particles involved in denitrification in the December 2011 Arctic stratosphere. *Atmos. Chem. Phys.* **16**, 9505–9532 (2016). URL https://doi.org/10.5194/acp-16-9505-2016.

[65] Théorêt, A. & Sandorfy, C. Infrared spectra and crystalline phase transitions of ammonium nitrate. *Can. J. Chem.* **42**, 57–62 (1964). URL https://doi.org/10.1139/v64-009.

[66] Fernandes, J. R., Ganguly, S. & Rao, C. Infrared spectroscopic study of the phase transitions in $CsNO_3$, $RbNO_3$ and $NH_4NO_3$. *Spectrochim. Acta A Mol. Biomol. Spectrosc.* **35**, 1013–1020 (1979). URL https://doi.org/10.1016/0584-8539(79)80001-X.

[67] Allen, D. T., Palen, E. J., Haimov, M. I., Hering, S. V. & Young, J. R. Fourier transform infrared spectroscopy of aerosol collected in a low pressure impactor (LPI/FTIR): Method development and field calibration. *Aerosol Sci. Technol.* **21**, 325–342 (1994). URL https://doi.org/10.1080/02786829408959719.

[68] Hopey, J. A., Fuller, K. A., Krishnaswamy, V., Bowdle, D. & Newchurch, M. J. Fourier transform infrared spectroscopy of size-segregated aerosol deposits on foil substrates. *Appl. Optics* **47**, 2266 (2008). URL https://doi.org/10.1364/AO.47.002266.

[69] Earle, M. E., Pancescu, R. G., Cosic, B., Zasetsky, A. Y. & Sloan, J. J. Temperature-dependent complex indices of refraction for crystalline $(NH_4)_2SO_4$. *J. Phys. Chem. A* **110**, 13022–13028 (2006). URL https://doi.org/10.1021/jp064704s.

[70] Rosenoern, T., Schlenker, J. C. & Martin, S. T. Hygroscopic growth of multicomponent aerosol particles influenced by several cycles of relative humidity. *J. Phys. Chem. A* **112**, 2378–2385 (2008). URL https://doi.org/10.1021/jp0771825.

[71] Laskina, O., Young, M. A., Kleiber, P. D. & Grassian, V. H. Infrared extinction spectra of mineral dust aerosol: Single components

and complex mixtures. *J. Geophys. Res.* **117** (2012). URL https://doi.org/10.1029/2012JD017756.

[72] Braban, C. F., Carroll, M. F., Styler, S. A. & Abbatt, J. P. D. Phase transitions of malonic and oxalic acid aerosols. *J. Phys. Chem. A* **107**, 6594–6602 (2003). URL https://doi.org/10.1021/jp034483f.

[73] Miñambres, L., Sánchez, M. N., Castaño, F. & Basterretxea, F. J. Hygroscopic properties of internally mixed particles of ammonium sulfate and succinic acid studied by infrared spectroscopy. *J. Phys. Chem. A* **114**, 6124–6130 (2010). URL https://doi.org/10.1021/jp101149k.

[74] Chasan, D. E. & Norwitz, G. Infrared determination of inorganic nitrates by the pellet technique; infrared determination of two inorganic nitrates in the presence of each other. *Appl. Spectrosc.* **24**, 283–287 (1970). URL https://doi.org/10.1366/000370270774371994.

[75] Harris, M. J., Salje, E. K. H. & Guttler, B. K. An infrared spectroscopic study of the internal modes of sodium nitrate: Implications for the structural phase transition. *J. Phys. Condens. Matter* **2**, 5517–5527 (1990). URL https://doi.org/10.1088/0953-8984/2/25/004.

[76] Ungermann, J. *et al.* CRISTA-NF measurements with unprecedented vertical resolution during the RECONCILE aircraft campaign. *Atmos. Meas. Tech.* **5**, 1173–1191 (2012). URL https://doi.org/10.5194/amt-5-1173-2012.

[77] Sutton, M. A., Erisman, J. W., Dentener, F. & Möller, D. Ammonia in the environment: From ancient times to the present. *Environ. Pollut.*

**156**, 583 – 604 (2008). URL https://doi.org/10.1016/j.envpol.2008.03.013.

[78] von Bobrutzki, K. *et al.* Field inter-comparison of eleven atmospheric ammonia measurement techniques. *Atmos. Meas. Tech.* **3**, 91–112 (2010). URL https://doi.org/10.5194/amt-3-91-2010.

[79] von Clarmann, T. *et al.* Retrieval of temperature, $H_2O$, $O_3$, $HNO_3$, $CH_4$, $N_2O$, $ClONO_2$ and ClO from MIPAS reduced resolution nominal mode limb emission measurements. *Atmos. Meas. Tech.* **2**, 159–175 (2009). URL https://doi.org/10.5194/amt-2-159-2009.

[80] Tikhonov, A. On the solution of incorrectly stated problems and method of regularization. *Dokl. Akad. Nauk. SSSR* **151**, 501–504 (1963).

[81] Woiwode, W. *et al.* Validation of first chemistry mode retrieval results from the new limb-imaging FTS GLORIA with correlative MIPAS-STR observations. *Atmos. Meas. Tech.* **8**, 2509–2520 (2015). URL https://doi.org/10.5194/amt-8-2509-2015.

[82] Johansson, S. *et al.* Airborne limb-imaging measurements of temperature, $HNO_3$, $O_3$, $ClONO_2$, $H_2O$ and CFC-12 during the Arctic winter 2015/16: characterization, in situ validation and comparison to Aura/MLS. *Atmos. Meas. Tech.* **11**, 4737–4756 (2018). URL https://doi.org/10.5194/amt-11-4737-2018.

[83] Brands, M. *et al.* Characterization of a newly developed aircraft-based laser ablation aerosol mass spectrometer (ALABAMA) and first field

deployment in urban pollution plumes over Paris during MEGAPOLI 2009. *Aerosol Sci. Technol.* **45**, 46–64 (2011). URL https://doi.org/10.1080/02786826.2010.517813.

[84] Murphy, D. M. & Thomson, D. S. Laser ionization mass spectroscopy of single aerosol particles. *Aerosol Sci. Technol.* **22**, 237–249 (1995). URL https://doi.org/10.1080/02786829408959743.

[85] Cairo, F. *et al.* A comparison of light backscattering and particle size distribution measurements in tropical cirrus clouds. *Atmos. Meas. Tech.* **4**, 557–570 (2011). URL https://doi.org/10.5194/amt-4-557-2011.

[86] Pisso, I. & Legras, B. Turbulent vertical diffusivity in the sub-tropical stratosphere. *Atmos. Chem. Phys.* **8**, 697–707 (2008). URL https://doi.org/10.5194/acp-8-697-2008.

[87] Tissier, A.-S. & Legras, B. Convective sources of trajectories traversing the tropical tropopause layer. *Atmos. Chem. Phys.* **16**, 3383–3398 (2016). URL https://doi.org/10.5194/acp-16-3383-2016.

[88] Wohltmann, I. & Rex, M. The Lagrangian chemistry and transport model ATLAS: validation of advective transport and mixing. *Geosci. Mod. Dev.* **2**, 153–173 (2009). URL https://doi.org/10.5194/gmd-2-153-2009.

# Acknowledgements

We acknowledge the Geophysica pilots and crew as well as the local support in Kathmandu. We are grateful to the instrument development and operation teams of GLORIA at KIT and Jülich, and of ERICA at MPI-C and IPA-JGU and to the technical team of AIDA at KIT. The work at KIT and Jülich was supported by the Helmholtz ATMO program. We would like to thank the teams at ULB/LATMOS (Université Libre de Bruxelles/Laboratoire Atmosphères, Milieux, Observations Spatiales) for provision of IASI $NH_3$ data. The European Space Agency (ESA) is acknowledged for MIPAS data provision. Meteorological analysis data have been provided by the European Centre for Medium-Range Weather Forecasts (ECMWF). ERA5 trajectories computations were generated using Copernicus Climate Change Service Information. D. Offermann and his team are acknowledged for conducting CRISTA observations in the AMA region. We thank M.L. Santee for helpful discussions on satellite datasets. Funding for the ERICA instrument development was provided by the European Research Council ERC Advanced Grant of S.Bo. (EXCATRO project, Grant No. 321040). Part of this work was supported by the European Community's Seventh Framework Programme (FP7/2007 - 2013) under grant agreement no. 603557, CEFIPRA5607-1, ANR-17-CE01-0015. We also thank the Aeris data infrastructure for providing access to the MSG1 and Himawari data.

# Author contributions

M.H. conducted the analysis of MIPAS and GLORIA data, produced Figs. 2–4, and wrote the paper with all authors contributing. J.U. conducted the analysis of CRISTA data, helped with analysis of GLORIA data and produced Fig. 1. A.D., S.M., A.B., O.A., A.H., and S.Bo. performed and analysed the aircraft in situ measurements of ERICA. C.M. and R.We. prepared the analyses for Fig. 4a, O.A. for Fig. 4b. C.M. and R.We. conducted the measurements and data analyses for UHSAS and COPAS, respectively. R.W., H.S., O.M., and T.L. conceived and performed the AIDA experiments and contributed to their interpretation. R.S. discovered the AN emission feature in CRISTA data for the first time. M.Ri. conceived the reanalysis of the CRISTA data wrt. signals of the ATAL. G.S. contributed to the analysis of MIPAS data. B.L. and S.Bu. conducted the TRACZILLA trajectory calculations. F.C. performed the MAS aircraft observations and conducted their analysis. F.F.V. conducted the GLORIA aircraft observations. S.J. analysed the trajectory datasets in combination with the IASI measurements. S.J. and L.K. helped with analysis of GLORIA data. P.P. contributed to the CRISTA and GLORIA data analysis. T.N. helped with performing the GLORIA observations. R.M. contributed to the interpretation of the observations. J.O. contributed to the interpretation of spectroscopic issues of AN and $NH_3$. F.S. and M.Re. defined the flight region, the general approach, general flight patterns and instrumentation of the aircraft campaign and organized it. I.W. developed the ATLAS model and provided the trajectory calculations from it, with contributions from M.Re.

# Corresponding author

Correspondence and requests for materials should be addressed to M.H. (michael.hoepfner@kit.edu).

# Competing interests

The authors declare no competing interests.

# Data availability

The datasets generated and analysed during the current study are available from the corresponding author on request. Additionally, the CRISTA dataset of ammonium nitrate is publicly available at: `https://datapub.fz-juelich.de/slcs/crista/an/`. MIPAS and GLORIA data of ammonia and ammonium nitrate as well as trajectory information and AIDA spectra can be downloaded from the KITopen archive at: https://doi.org/?. IASI data on $NH_3$ are available at `http://iasi.aeris-data.fr/NH3/`.

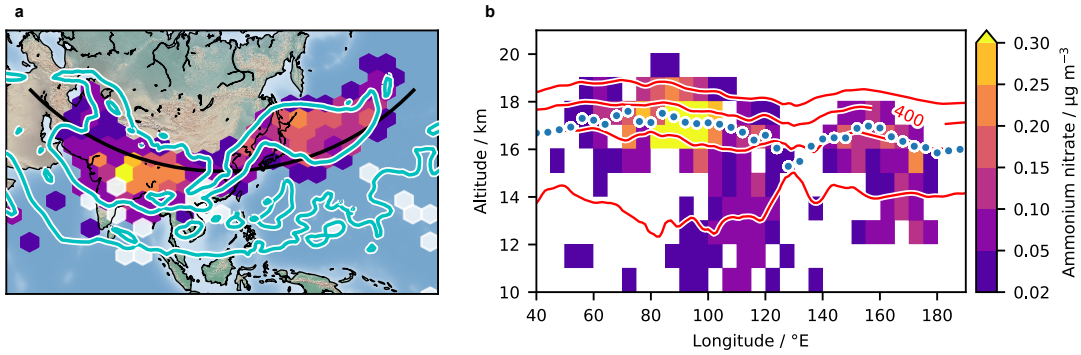


Fig. 1: **Ammonium nitrate observed by CRISTA in the UT 1997.** Cross sections of synoptically interpolated AN mass concentrations, **a**, at 380 K potential temperature (16–17 km altitude), as well as, **b**, at 30°N derived from CRISTA observations between 8 and 16 August 1997. The cyan line in panel **a** shows the 4.1 PVU potential vorticity contour line, a rough measure for the extent of the AMA core, white hexagons indicate missing data and the black line the position of the cross-section of panel **b**. Red lines in panel **b** show potential temperature (K) and blue dots the location of the lapse rate tropopause.

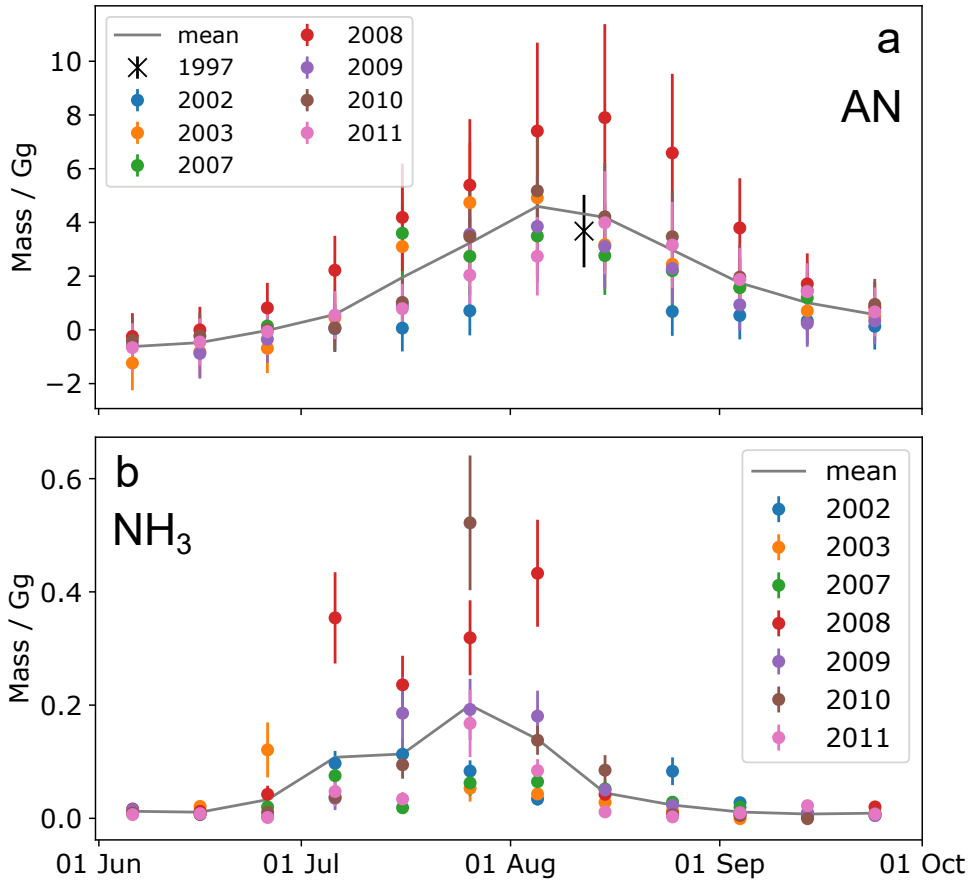


Fig. 2: **Time series of AN and $NH_3$ in the AMA.** Time series of total mass of **a**, AN, and **b**, $NH_3$ as derived from MIPAS observations for the region 10°E–110°E, 20°N–40°N and 13–17 km altitude. CRISTA observations of AN are included in **a** as a black cross. Error bars are Gaussian combinations of the estimated retrieval errors (see Methods) and the standard deviations of the mean values.

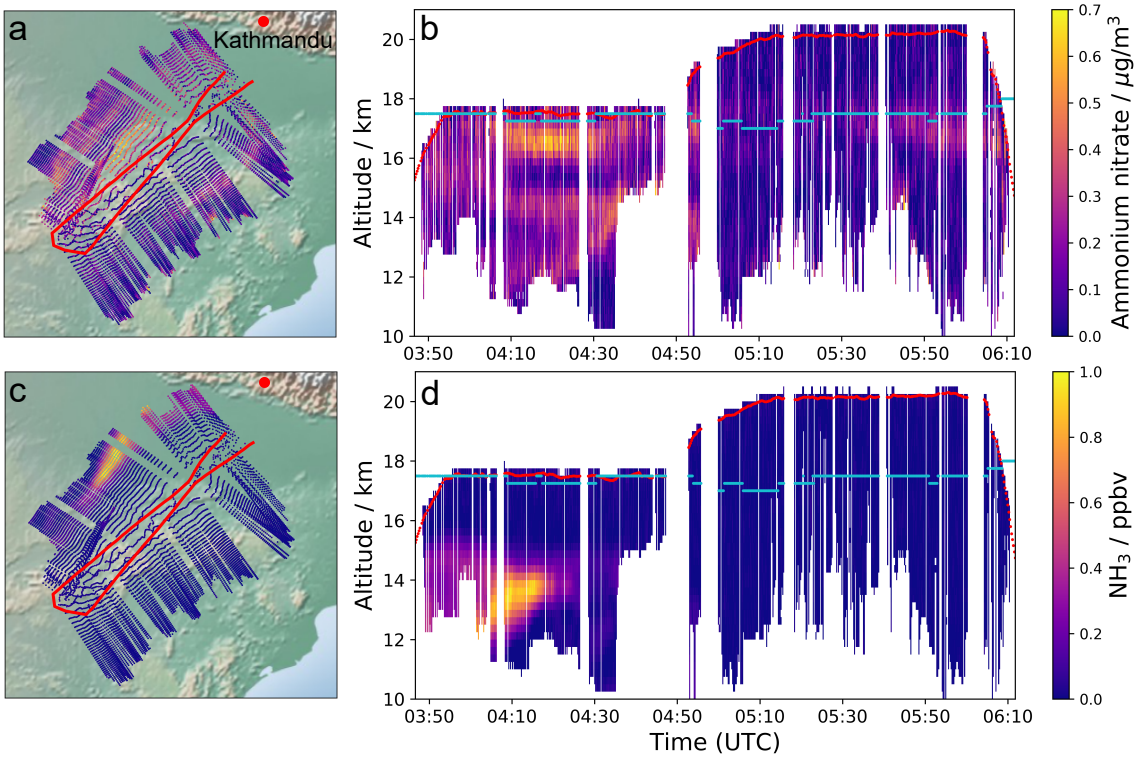


Fig. 3: **Airborne limb-imaging observations of AN and $NH_3$ in the UT above India during the 2017 Asian monsoon season.** **a**,**b**, altitude-time horizontal projections of AN mass densities, and **c**,**d**, $NH_3$ volume mixing ratios derived from GLORIA measurements during the Geophysica flight on 31 July 2017. Horizontal projection at tangent points (**a**,**c**) and vertical projection (b,d). Vertical resolution and estimated uncertainty (precision, accuracy): AN: 0.8 km, $\pm 0.03\,\mu g\,m^{-3}$ $\pm 30\%$; $NH_3$: 0.8 km, $\pm 8$ pptv $\pm 20\%$; . Red lines: aircraft position (**a**,**c**) and altitude (**b**,**d**), light blue lines (**b**,**d**): lapse rate tropopause.

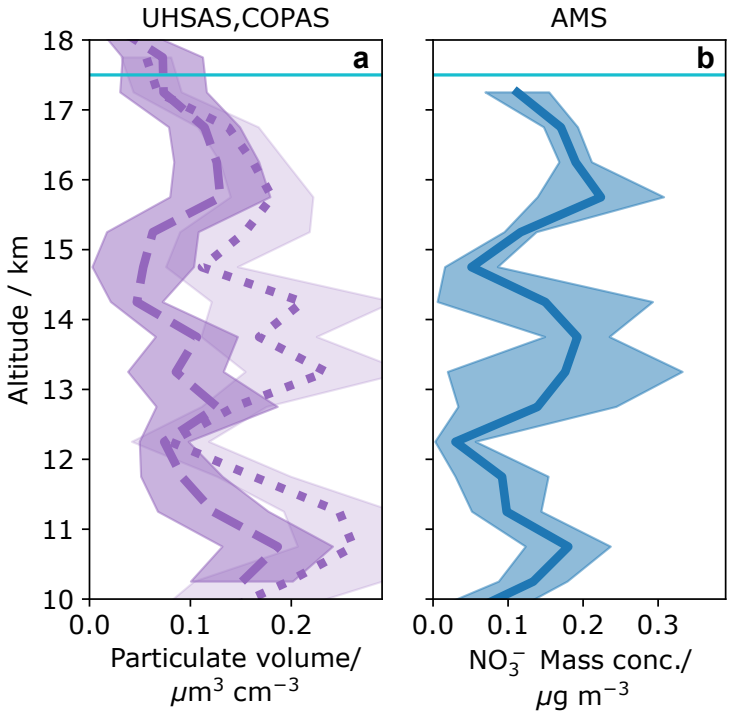


Fig. 4: **Airborne in-situ aerosol observations in the Asian monsoon UT on 31 July 2017. a**, UHSAS and COPAS derived aerosol volume density during ascent (dashed) and descent (dotted) at Kathmandu. **b**, ERICA-AMS particulate $NO_3^-$ mass concentrations. The values are averages in vertical bins of 0.25 km. For the nitrate content of ERICA-AMS, the uncertainty is estimated to 30%. The estimated uncertainty of the UHSAS and COPAS data is below 30%. Light blue lines indicate the lapse rate tropopause.

# Ammonium nitrate particles formed in upper troposphere sourced from ground ammonia during Asian monsoons

Michael Höpfner[1], Jörn Ungermann[2], Stephan Borrmann[3,4], Robert Wagner[1], Reinhold Spang[2], Martin Riese[2,5], Gabriele Stiller[1], Oliver Appel[3,4], Anneke M. Batenburg[3,4], Silvia Bucci[6], Francesco Cairo[7], Antonis Dragoneas[3,4], Felix Friedl-Vallon[1], Andreas Hünig[3,4], Sören Johansson[1], Lukas Krasaukas[2], Bernard Legras[6], Thomas Leisner[1], Christoph Mahnke[3,4], Ottmar Möhler[1], Sergej Molleker[3,4], Rolf Müller[2], Tom Neubert[8], Johannes Orphal[1], Peter Preusse[2], Markus Rex[9], Harald Saathoff[1], Fred Stroh[2], Ralf Weigel[4], and Ingo Wohltmann[9]

[1]Institute of Meteorology and Climate Research, Karlsruhe Institute of Technology, Karlsruhe, Germany
[2]Institute of Energy and Climate Research, Stratosphere, Forschungszentrum Jülich, Jülich, Germany
[3]Department for Particle Chemistry, Max Planck Institute for Chemistry, Mainz, Germany
[4]Institute for Atmospheric Physics, Johannes Gutenberg University, Mainz, Germany
[5]Institute for Atmospheric and Environmental Research, University of Wuppertal, Wuppertal, Germany
[6]Laboratoire de Météorologie Dynamique, UMR8539, IPSL, CNRS/PSL-ENS/Sorbonne Université/École polytechnique, Paris, France
[7]Institute of Atmospheric Sciences and Climate, ISAC-CNR, Rome, Italy
[8]Central Institute of Engineering, Electronics and Analytics - Electronic Systems, Forschungszentrum Jülich, Jülich, Germany
[9]Alfred Wegener Institute, Helmholtz Center for Polar and Marine Research, Potsdam, Germany

## Supplementary discussion of the AIDA cloud chamber observations

Supplementary Figure 1 shows the infrared spectrum of supercooled liquid AN solution droplets in the regime of the $\nu_2(NO_3^-)$ absorption band (blue line), which was recorded after nebulization of the 100 mol% AN solution, drying of the aerosol flow to RH $\leq$ 3%, and injection into the AIDA chamber at 61% RH and 223 K. The complete mid-infrared spectrum (shown as trace A in Supplementary Fig. 2, top panel: 6000–800 $cm^{-1}$, lower panel: expanded view from 1600 to 800 $cm^{-1}$) proves the liquid phase of the injected aerosol particles by showing the characteristic infrared signature of liquid water centred at about 3500 $cm^{-1}$ [1, 2]. Furthermore, the recorded depolarization ratio of the aerosol particles at 488 nm and 178° scattering angle (see Methods) was less than 1%, as indicative of spherical, aqueous solution droplets. The strategy of this experiment was similar to the one adopted by [1], namely to confirm the crystallization of AN by exploiting the hysteresis effect in the deliquescence and efflorescence behaviour. According to the Aerosol Inorganics Model (AIM), the deliquescence relative humidity (DRH) of AN at 223 K is 97% [3]. If the AN solution droplets had fully crystallized at $\leq$ 3% RH prior to the injection into the AIDA vessel, the particles should not have taken up any liquid water in the chamber, given that the prevalent RH was well below the DRH. The AN particles were kept for an observation period of almost four hours in the AIDA chamber at 223 K and 61% RH, without showing any increase in the depolarization ratio or change in the infrared spectral signature. Our experiment thus corroborates previous studies that have demonstrated the strong inhibition of efflorescence for pure AN solution droplets [4, 5, 1]. The infrared spectrum of liquid AN (Supplementary Fig. 1), however, clearly fails to reproduce the measurement by the CRISTA limb-sounder.

Whereas pure AN solution droplets have a strong tendency to remain in the supercooled liquid state, the crystallization of AN is facilitated by impurities in the aqueous solutions [5], the presence of insoluble inclusions like mineral dust [6], and/or the admixture of compounds that easily crystallize and thereby serve as heterogeneous nuclei to promote the formation of solid AN [1]. Additionally, contact efflorescence initiated by externally located solid particles has been established as a pathway for the crystallization of supersaturated aqueous AN particles [7]. Internal mixtures of ammonium, nitrate, and sulfate are considered as a common

aerosol particle type in the troposphere, and their crystallization behaviour has been thoroughly investigated in aerosol flow tube studies conducted at room temperature [1, 8]. For example, it was shown that the addition of just 10 mol% ammonium sulfate (AS) promoted the crystallization of AN in mixed AN/AS solution droplets [1]. We were able to reproduce this finding in our AIDA experiments. When using a 90 mol% AN + 10 mol% AS bulk solution for aerosol generation, the infrared spectrum of the injected particles (Supplementary Fig. 2, trace C) was devoid of any liquid water signature. Instead, the spectral changes in the band system between 1500 and 1300 $cm^{-1}$ as well as the appearance of the sharp peak at 831 $cm^{-1}$ indicated the presence of crystalline AN. In accordance with the prevalence of crystalline particles, the back-scattering linear depolarization ratio adopted a value of 17%. The sulfate admixture was seen by the absorption band at about 1100 $cm^{-1}$, which can be due to pure crystalline AS or the double salts 2AN·AS and 3AN·AS [9, 1].

We also investigated whether smaller admixtures of AS were still sufficient to trigger the crystallization of mixed AN/AS solution droplets. As shown by spectrum B in Supplementary Fig. 2 , we were able to produce crystalline AN particles even for an AS mole fraction as low as 2.9 mol%. For this mixture, however, the AIDA chamber had to be kept at a lower RH (22%) in order to observe the instantaneous formation of crystalline particles upon aerosol injection. When the AIDA chamber was kept at 61% RH, the injected aerosol particles generated from the 97.1 mol% AN + 2.9 mol% AS bulk solution initially showed the infrared signature representative of supercooled solution droplets with a depolarization ratio $< 1\%$. In contrast to the experiment with pure AN solution droplets, the mixed AN/AS particles gradually crystallized while suspended in the AIDA chamber at 223 K and 61% RH for four hours, as evidenced by an increase of the depolarization ratio from $< 1$ to 5% and a concomitant change of the infrared spectral signature. Spectrum D in Supplementary Fig. 2 illustrates the difference in the spectral signature after the observation time of four hours, demonstrating the formation of the crystalline AN phase. From the infrared spectra, we estimated that about 25% of the aerosol population had crystallized within four hours of observation. Supplementary Figure 1 demonstrates that the $\nu_2(NO_3^-)$ band of crystalline AN recorded in the AIDA chamber (orange line, enlarged view of spectrum B from Supplementary Fig. 2) shows a very good match with the CRISTA observation. To the best of our knowledge, the AIDA spectrum represents the first infrared measurement of suspended, crystalline AN particles at temperature conditions of the UT. The crystallization experiments underline that small amounts of sulfate impurities are sufficient to enable the formation of the

solid phase of AN.

Trace E in Supplementary Fig. 2 (bottom) shows the previously recorded infrared spectrum of crystalline AN/AS particles with 10 mol% AS at room temperature [1]. In comparison with the corresponding AIDA spectrum recorded at 223 K (trace C), there are small changes in the fine structure of the band system between 1500 and 1300 $cm^{-1}$ with contributions from the $\nu_4(NH_4^+)$ and $\nu_3(NO_3^-)$ modes. These spectral changes could be indicative of a thermal phase transition, given that five different phases of crystalline AN have been reported at ambient pressure [10, 11]. In particular, the phase transition from phase IV to V, which is supposed to occur at 255 K, could account for the temperature-dependent changes in the spectral habitus at 1500 –1300 $cm^{-1}$. In contrast to this wavenumber regime, previous infrared studies with thin films of AN have shown that the peak position of the $\nu_2(NO_3^-)$ mode is rather insensitive to the transition between phase IV and V [12, 13, 14]. This is corroborated by our findings shown in the left part of Supplementary Fig. 3, where we show the spectral regime of the $\nu_2$ band of AN particles in the liquid and solid phase recorded during the AIDA experiments at 223 K and the flow-tube studies performed at 293 K by [1]. Obviously, the spectral habitus of the $\nu_2(NO_3^-)$ mode does not change with temperature, both for the liquid and the solid phase.

As outlined in the Methods section, the infrared optical depths recorded could be quantitatively scaled by the mass concentration of the suspended aerosol particles, thereby yielding mass specific absorption coefficients of the $\nu_2(NO_3^-)$ mode of AN. A representative volume size distribution of the aerosol particles from the crystallization experiment with 97.1 mol% AN + 2.9 mol% AS at 223 K and 22% RH, which was used to derive the aerosol mass concentration, is shown in the right part of Supplementary Fig. 3.

# References


[1] Schlenker, J. C. & Martin, S. T. Crystallization pathways of sulfate-nitrate-ammonium aerosol particles. *J. Phys. Chem. A* **109**, 9980–9985 (2005). URL https://doi.org/10.1021/jp052973x.

[2] Schuttlefield, J., Al-Hosney, H., Zachariah, A. & Grassian, V. H. Attenuated total reflection fourier transform infrared spectroscopy to investigate water uptake and phase transitions in atmospherically relevant particles. *Appl. Spectrosc.* **61**, 283–292 (2007). URL https://doi.org/10.1366/000370207780220868.

[3] Clegg, S. L., Brimblecombe, P. & Wexler, A. S. Thermodynamic model of the system $H^+$-$NH_4^+$-$SO_4^{2-}$-$NO_3^-$-$H_2O$ at tropospheric temperatures. *J. Phys. Chem. A* **102**, 2137–2154 (1998). URL https://doi.org/10.1021/jp973042r.

[4] Cziczo, D. J. & Abbatt, J. P. D. Infrared observations of the response of NaCl, $MgCl_2$, $NH_4HSO_4$, and $NH_4NO_3$ aerosols to changes in relative humidity from 298 to 238 K. *J. Phys. Chem. A* **104**, 2038–2047 (2000). URL https://doi.org/10.1021/jp9931408.

[5] Lightstone, J. M., Onasch, T. B., Imre, D. & Oatis, S. Deliquescence, efflorescence, and water activity in ammonium nitrate and mixed ammonium nitrate/succinic acid microparticles. *J. Phys. Chem. A* **104**, 9337–9346 (2000). URL https://doi.org/10.1021/jp002137h.

[6] Han, J.-H., Hung, H.-M. & Martin, S. T. Size effect of hematite and corundum inclusions on the efflorescence relative humidities of aqueous ammonium nitrate particles. *J. Geophys. Res.* **107**, AAC 3–1–AAC 3–9 (2002). URL https://doi.org/10.1029/2001JD001054.

[7] Davis, R. D., Lance, S., Gordon, J. A., Ushijima, S. B. & Tolbert, M. A. Contact efflorescence as a pathway for crystallization of atmospherically relevant particles. *Proc. Natl. Acad. Sci. U.S.A.* **112**, 15815–15820 (2015). URL https://doi.org/10.1073/pnas.1522860113.

[8] Schlenker, J. C., Malinowski, A., Martin, S. T., Hung, H.-M. & Rudich, Y. Crystals formed at 293 K by aqueous sulfate-nitrate-ammonium-proton aerosol particles. *J. Phys. Chem. A* **108**, 9375–9383 (2004). URL https://doi.org/10.1021/jp047836z.

[9] Bothe, J. R. & Beyer, K. D. Experimental determination of the $NH_4NO_3$/$(NH_4)_2SO_4$/$H_2O$ phase diagram. *J. Phys. Chem. A* **111**, 12106–12117 (2007). URL https://doi.org/10.1021/jp0760859. PMID: 17994714.

[10] Chellappa, R. S., Dattelbaum, D. M., Velisavljevic, N. & Sheffield, S. The phase diagram of ammonium nitrate. *J. Chem. Phys.* **137**, 064504 (2012). URL https://doi.org/10.1063/1.4733330.

[11] Herrmann, M. J. & Engel, W. Phase transitions and lattice dynamics of ammonium nitrate. *Propellants Explos. Pyrotech.* **22**, 143–147 (1997). URL https://doi.org/10.1002/prep.19970220308.

[12] Fernandes, J. R., Ganguly, S. & Rao, C. Infrared spectroscopic study of the phase transitions in $CsNO_3$, $RbNO_3$ and $NH_4NO_3$. *Spectrochim. Acta A Mol. Biomol. Spectrosc.* **35**, 1013–1020 (1979). URL https://doi.org/10.1016/0584-8539(79)80001-X.

[13] Koch, T. G., Holmes, N. S., Roddis, T. B. & Sodeau, J. R. Low-temperature reflection/absorption IR study of thin films of nitric acid hydrates and ammonium nitrate adsorbed on gold foil. *J. Chem. Soc. Faraday Trans.* **92**, 4787 (1996). URL https://doi.org/10.1039/FT9969204787.

[14] Théorêt, A. & Sandorfy, C. Infrared spectra and crystalline phase transitions of ammonium nitrate. *Can. J. Chem.* **42**, 57–62 (1964). URL https://doi.org/10.1139/v64-009.

[15] Offermann, D. *et al.* Cryogenic Infrared Spectrometers and Telescopes for the Atmosphere (CRISTA) experiment and middle atmosphere variability. *J. Geophys. Res.* **104**, 16311–16325 (1999). URL https://doi.org/10.1029/1998JD100047.

## Supplementary Figures 1–11

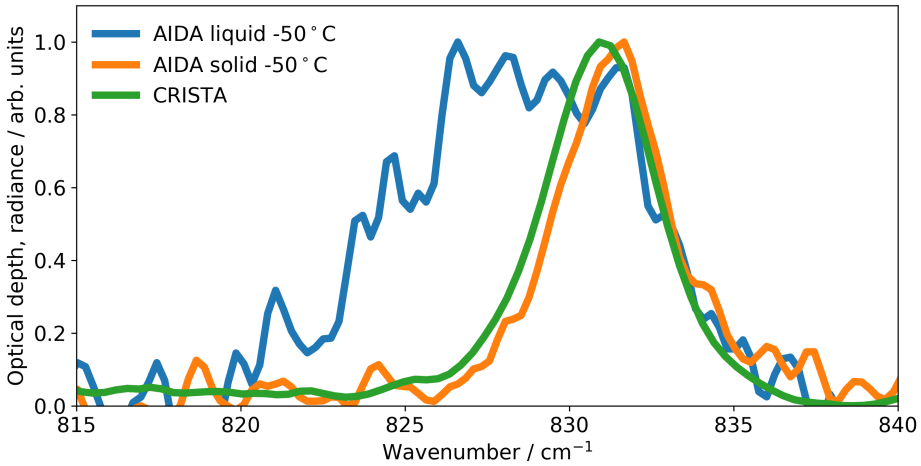


Supplementary Figure 1: **Infrared spectra of AN.** The $\nu_2(NO_3^-)$ infrared band of AN as observed in laboratory (AIDA) and inside the AMA by the CRISTA satellite instrument [15]. The CRISTA signal with 1.5 cm$^{-1}$ spectral resolution has been derived from all spectra measured during the flight in August 1997 within a tangent altitude range of 16–18 km, 20°–50°N and 30°–180°E (see Methods). The laboratory spectra of optical depth (liquid AN: blue, solid AN: orange) and the satellite radiances (green) are scaled and offset to facilitate their comparison.

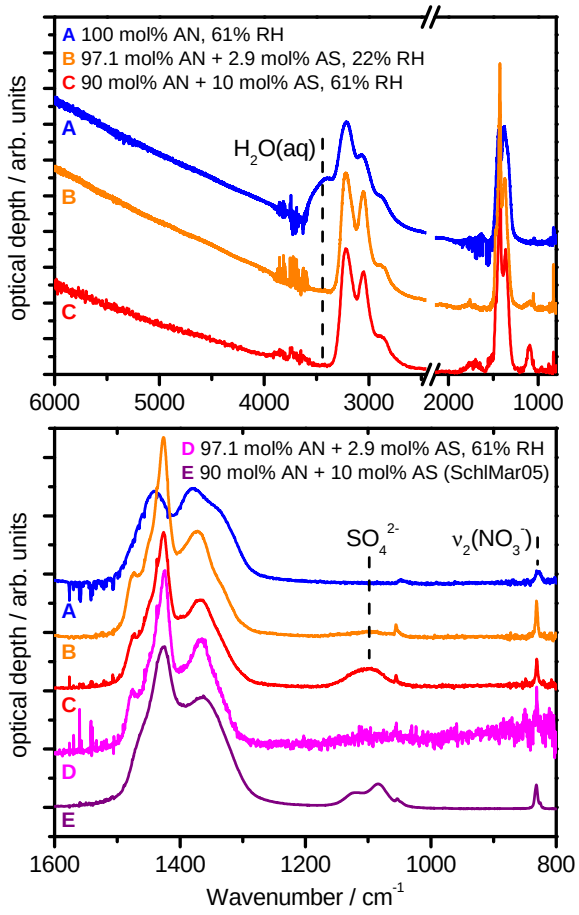


Supplementary Figure 2: **AIDA laboratory spectra of liquid and solid AN particles.** Mid-infrared spectra of aerosol particles composed of AN and mixtures of AN and AS. Top panel: Spectral regime from 6000 to 800 $cm^{-1}$ (with $CO_2$ absorption regime between 2450 and 2150 $cm^{-1}$ excluded). Bottom panel: Expanded view from 1600 to 800 $cm^{-1}$. Spectra A to D were recorded at 223 K in the AIDA chamber, whereas spectrum E, recorded at 293 K, was taken from the literature [1]. All spectra were scaled and offset to facilitate their comparison. See Supplementary discussion for details.

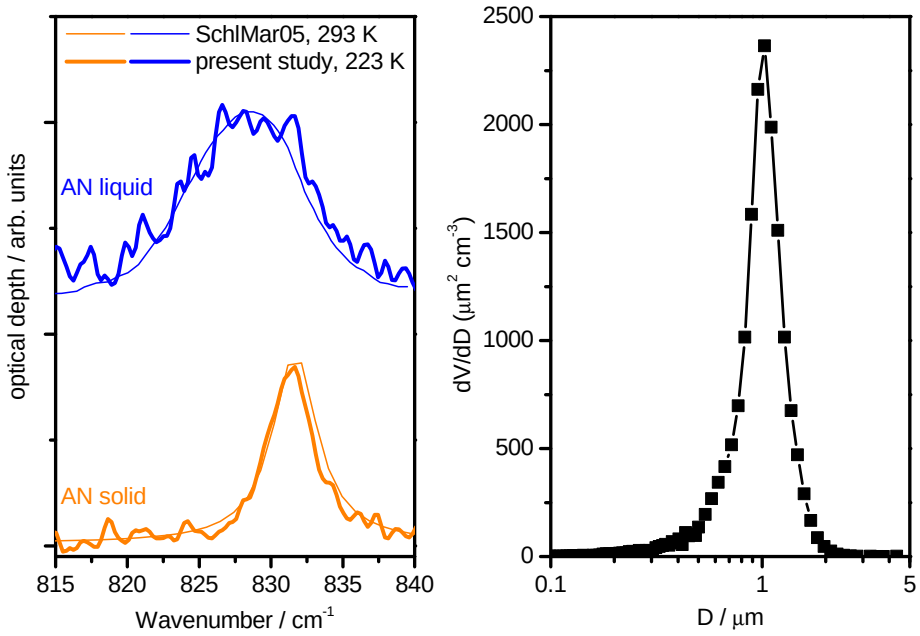


Supplementary Figure 3: **Comparison of laboratory spectra of liquid and solid AN and volume size distribution.** Left panel: Comparison of the $\nu_2(NO_3^-)$ infrared absorption mode of liquid and solid AN particles, recorded at 223 K during the present AIDA experiments (expanded view of spectra A and B from Supplementary Fig. 2) and at 293 K during previous aerosol flow-tube experiments ("SchlMar05", digitized graphs from the inserts in Figs. 2 and 5 of [1]). All spectra were scaled and offset to facilitate their comparison. Right panel: Volume-size distribution of crystalline aerosol particles generated from the 97.1 mol% AN + 2.9 mol% AS bulk solution after injection into the AIDA chamber at 223 K and 22% RH.

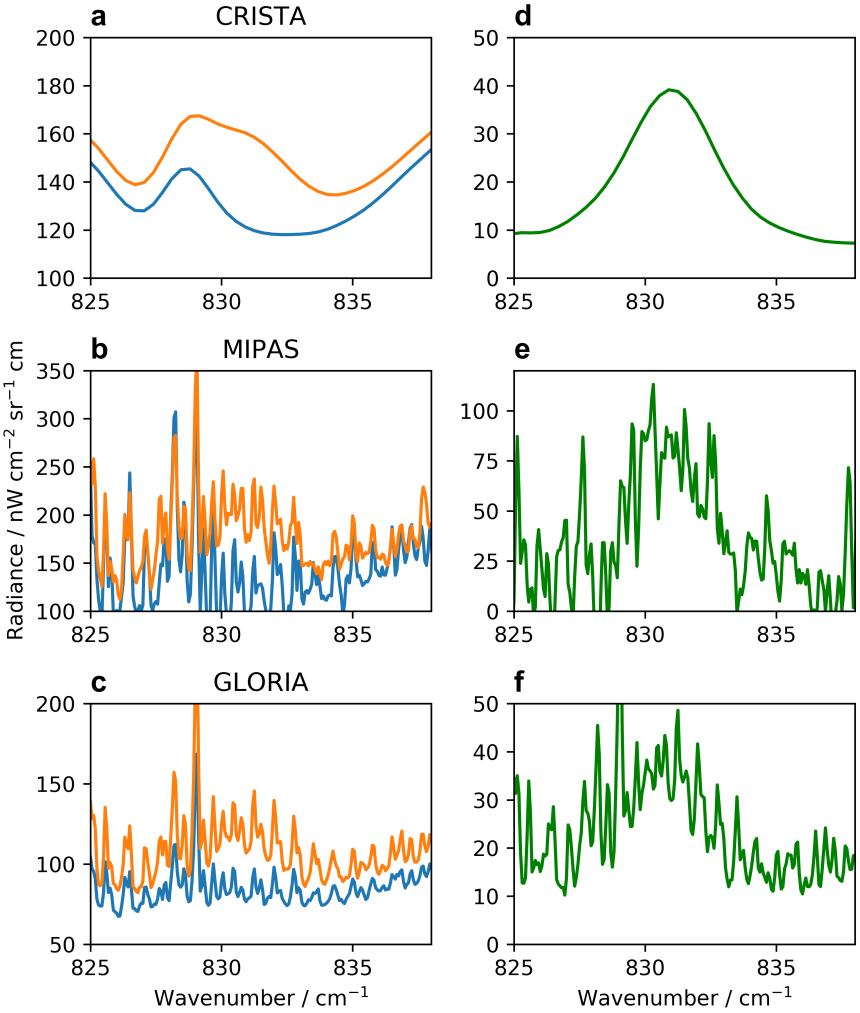


Supplementary Figure 4: **Detection of the $\nu_2$(NO$_3^-$) infrared band of ammonium nitrate in infrared limb spectra.** Measured spectra with (orange) and without (blue) the spectral band of AN and their difference (green). The spectra have been taken from observations obtained at different locations with high and low concentrations of AN, respectively. **a**,**d**, CRISTA data are averaged spectra selected over the whole Space Shuttle flight in August 1997 within a tangent altitude range of 16–18 km, 20–50° latitude and 30–180° longitude. **b**,**e**, MIPAS spectra between 15 km and 16 km tangent altitude from 8 August 2008, 7:15:30 UTC (orange) and 3:52:17 UTC (blue). **c**,**f**, mean GLORIA spectra from flight 31 July 2017 at tangent altitudes between 16.5 and 16.75 km at 4:15–4:21 UTC (orange) and 3:55–3:59 UTC (blue).

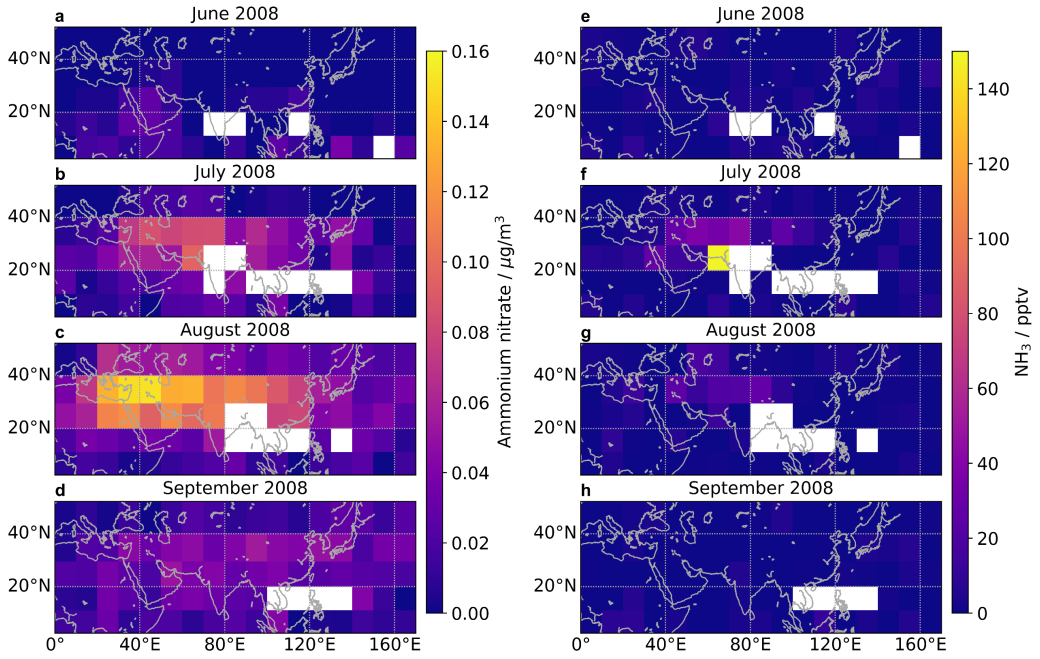


Supplementary Figure 5: **Ammonium nitrate and ammonia observed by MIPAS in the UT during the Asian monsoon 2008.** Monthly mean AN mass concentrations (**a**–**d**) and $NH_3$ volume mixing ratios (**e**–**h**) at 16 km altitude derived from MIPAS observations from June to September 2008. Data are monthly averages of single retrieved profiles within a 10° latitude × 10° longitude grid.

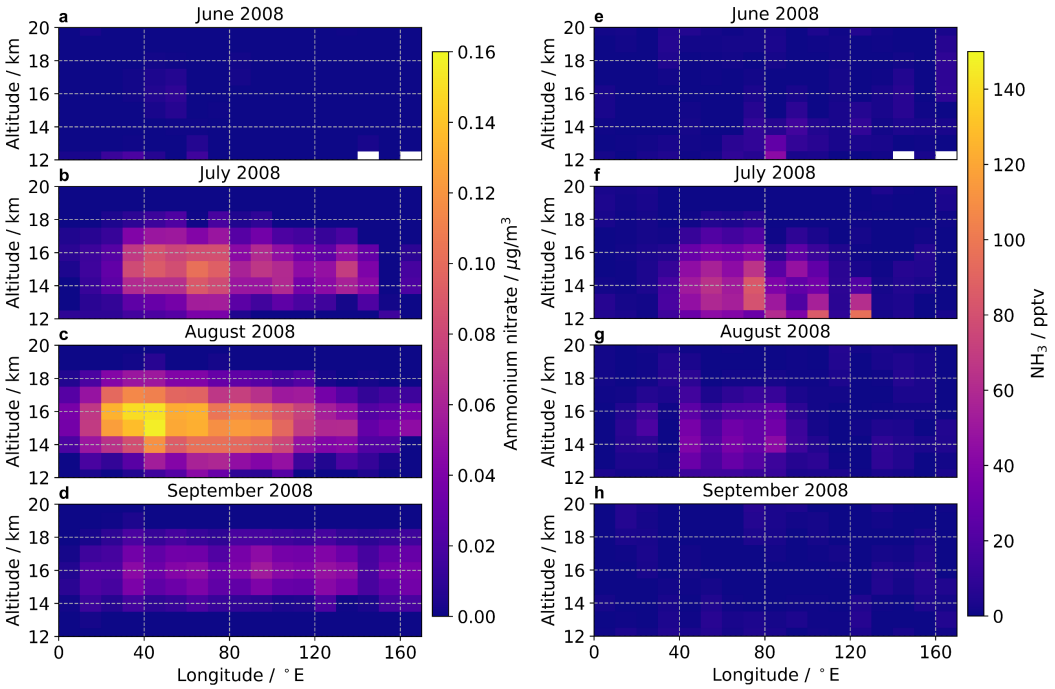


Supplementary Figure 6: **Ammonium nitrate and ammonia observed by MIPAS in the UT during the Asian monsoon 2008.** Monthly mean AN mass concentrations (**a**–**d**) and $NH_3$ volume mixing ratios (**e**–**h**) at $30$–$40^{\circ}$N derived from MIPAS observations from June to September 2008. Data are monthly averages of single profiles within a 10° latitude $\times$ 10° longitude grid.

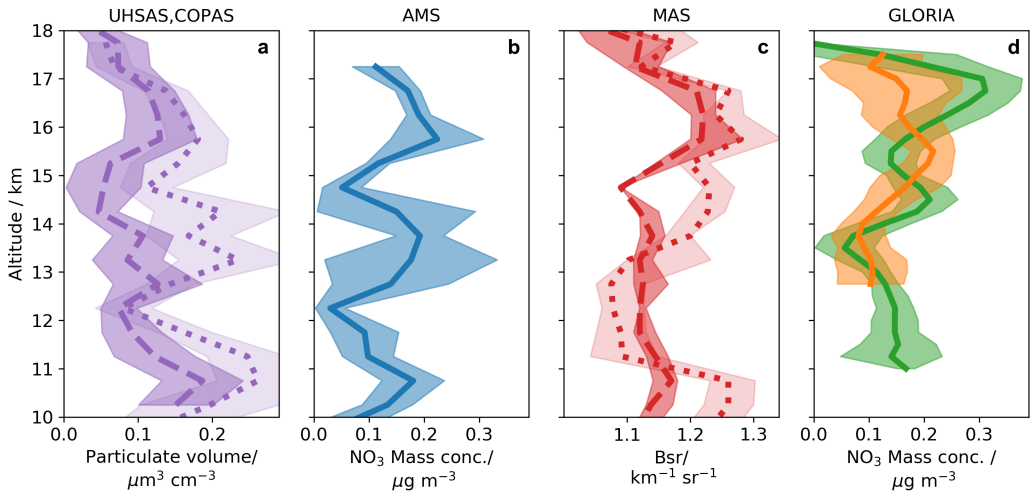


Supplementary Figure 7: **Airborne aerosol observations in the Asian monsoon UT on 31 July 2017. a**, UHSAS and COPAS derived aerosol volume density during ascent (dashed) and descent (dotted). **b**, ERICA-AMS particulate $NO_3^-$ mass concentrations. **c**, MAS backscatter ratios (Bsr) at 532 nm during ascent (dashed) and descent (dotted). **d**, GLORIA $NO_3^-$ mass concentration profiles from AN retrievals. **a**–**c**, have been obtained during ascent and descent at Kathmandu. The values are averages in vertical bins of 0.25 km. GLORIA data are mean profiles averaged during the flight between 3:50–3:55 UTC (orange) and between 4:05-4:10 UTC (green). Shaded areas indicate 25 and 75 percentiles for MAS and standard deviations in case of the other datasets. For the nitrate content of ERICA-AMS, the uncertainty is estimated to 30%. The estimated uncertainty of the UHSAS and COPAS data is below 30%. The uncertainty of MAS Bsr is estimated to 0.05. The estimated accuracy of the GLORIA data is 30%.

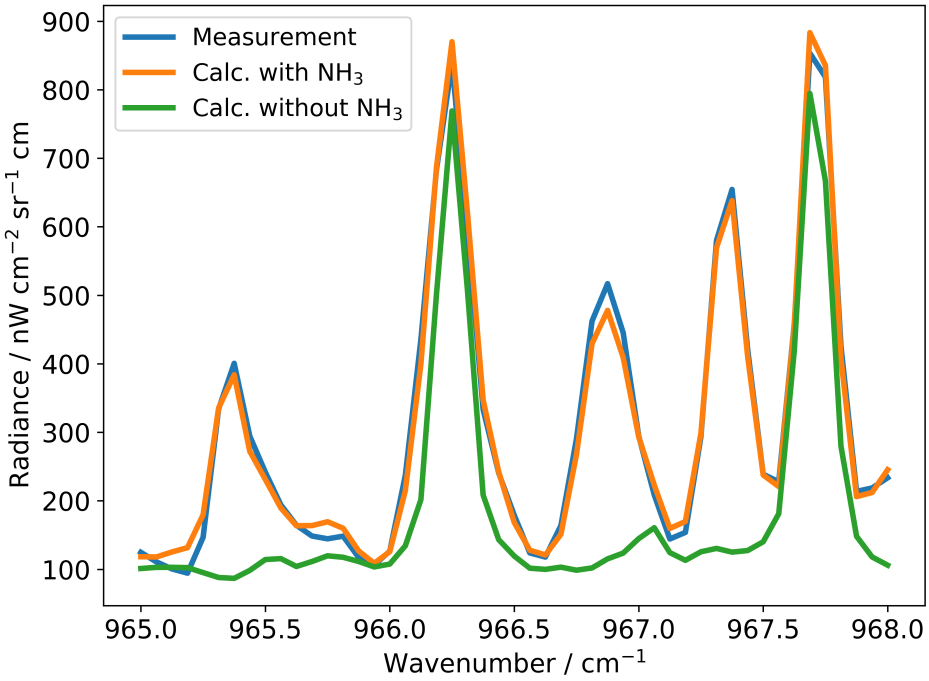


Supplementary Figure 8: **Detection of $NH_3$ emission lines in GLORIA limb infrared spectra.** Example of a GLORIA spectrum at a tangent height of 13.7 km on 31 July 2017, 4:15 UTC (blue) in comparison to the spectral fit including $NH_3$ spectral lines (orange) and a calculation without consideration of $NH_3$ (green). The two strongest lines belong to $CO_2$.

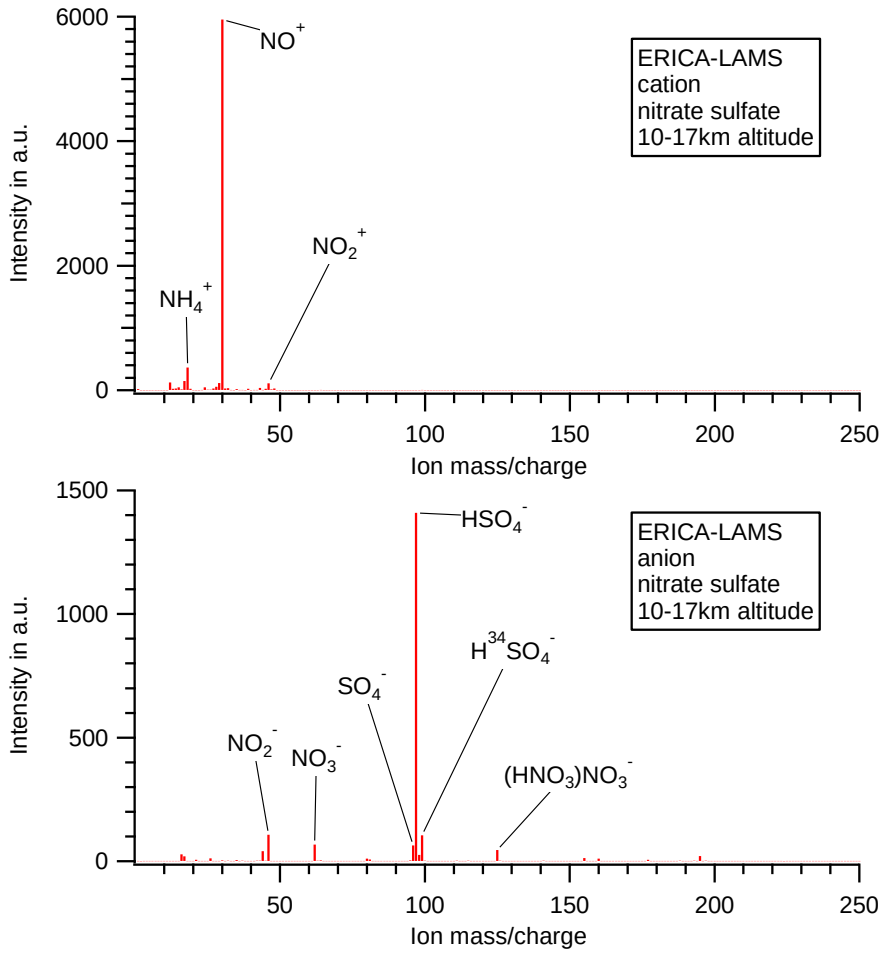


Supplementary Figure 9: **Particles containing nitrate and sulfate.** Average single particle mass spectra taken by ERICA-LAMS during the whole StratoClim campaign with simultaneously present spectral lines of sulfate and nitrate ions indicating that the individual particles of this category contain both, sulfate and nitrate components.

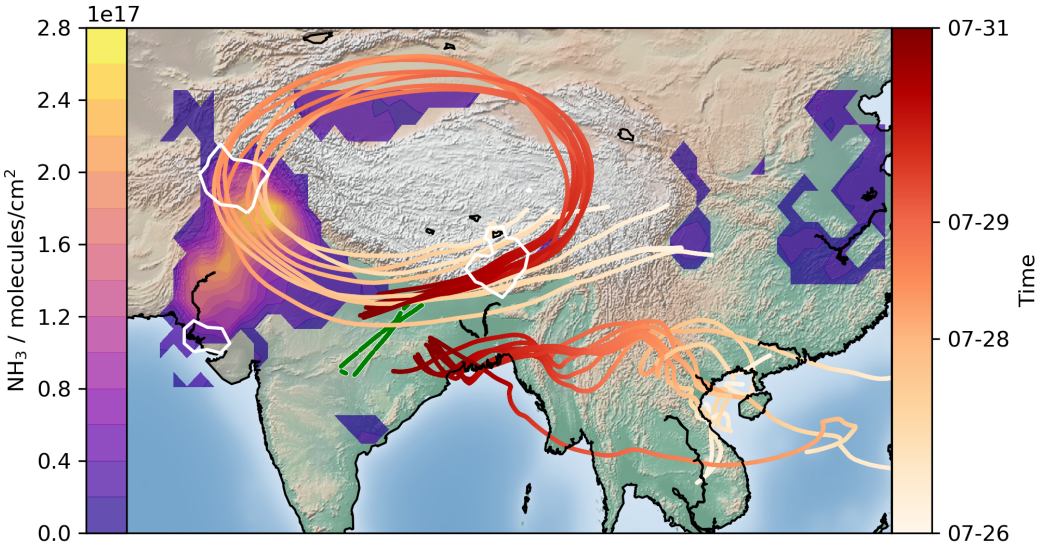


Supplementary Figure 10: **The origin of high $NH_3$ concentrations in the UT.** Exemplary subsets of backward TRACZILLA trajectories starting at GLORIA observations with enhanced $NH_3$ concentrations (SW-bound flight leg) and at no $NH_3$ enhancement (NE-bound leg) on 31 July 2017. The trajectories are colour-coded according to time. White contour lines highlight regions where the density of convective events, for the $NH_3$-enhancement trajectories release, is larger than 0.5%. This quantity is computed as the ratio, on a $1^\circ$ latitude $\times$ $1^\circ$longitude grid, of the number of encountered convective events with respect to the total number of released trajectories. Mean IASI column amounts of $NH_3$ for the time period 26–30 July 2017 are indicated by the colours of the left colour bar. IASI measurements less than 5% of the maximum value are not plotted. The aircraft flight path is shown as a green line.

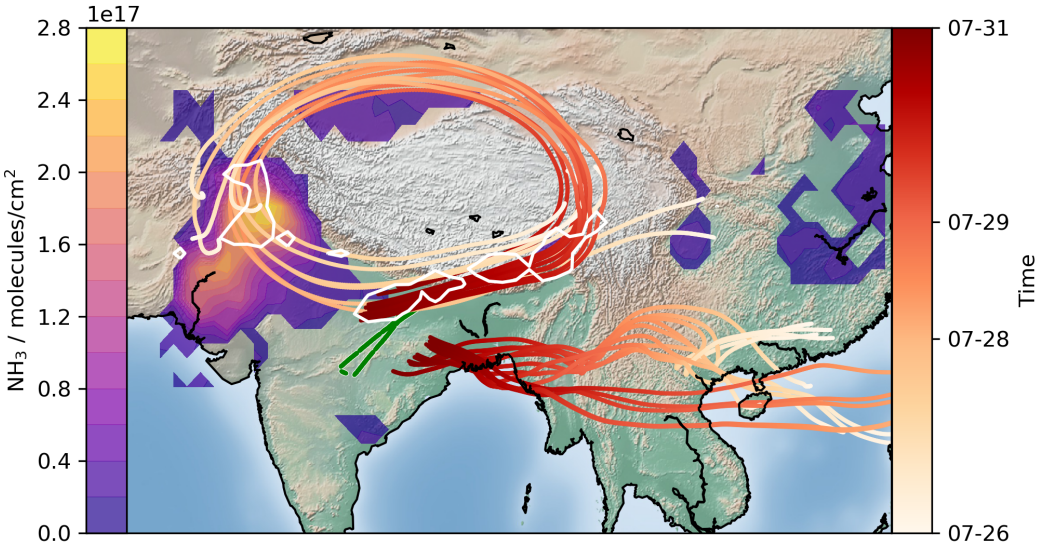


Supplementary Figure 11: **The origin of high $NH_3$ concentrations in the UT.** Same as Supplementary Fig. 10, but with trajectory data from the ATLAS model.